Rhythmic coordination of hippocampal-prefrontal ensembles for odor-place associative memory and decision making

Authors: Claire A. Symanski[1], John H. Bladon[2], Emi T. Kullberg[2] and Shantanu P. Jadhav[1,2,3]*

Affiliations:

[1]Graduate Program in Neuroscience, Brandeis University, Waltham, MA, 02453, USA

[2]Neuroscience Program, Department of Psychology, Volen National Center for Complex Systems, Brandeis University, Waltham, MA, 02453, USA

[3]Lead Contact

*Correspondence to: shantanu@brandeis.edu (S.P.J.)

ABSTRACT

Memory-guided decision making involves long-range coordination across sensory and cognitive brain networks, with key roles for the hippocampus and prefrontal cortex (PFC). To investigate coordination mechanisms that mediate sensory-cued decision making based on learned associations, we monitored activity in hippocampus (CA1), PFC, and olfactory bulb in rats performing an odor-place associative memory and decision task on a T-maze. During odor sampling, the beta (15-30 Hz) and respiratory (7-8 Hz) rhythms (RR) were prominent and coherent across the three regions, with beta specifically linked to fast decisions. Single neurons and ensembles in both CA1 and PFC encoded and predicted animals' upcoming choices, with choice-encoding dynamics linked specifically with beta rhythm coordination. Beta phase modulation of CA1 interneuron activity was linked to accurate decisions, suggesting a mechanism for enabling temporal coordination. Our findings indicate that beta rhythm coordination within the hippocampal-prefrontal network supports utilization of odor cues for memory-guided decision making.

KEYWORDS

Hippocampus; Prefrontal cortex; Beta oscillations; Respiratory rhythm; Phase locking; Decision making; Olfactory Bulb

INTRODUCTION

The ability to recall associations from memory and use them to guide behavior is a key aspect of cognition across species. Animals can associate sensory cues in the environment with rewarding and noxious experiences and utilize these cues for adaptive behavior. Memory-guided decision making demonstrates the brain's remarkable ability to link familiar cues with actions and beneficial outcomes, but little is known about the mechanisms responsible for this cognitive function.

Neurons that encode learned associations and reflect upcoming choice behavior have been reported in multiple regions in different sensory modalities[1-14]. However, sensory cued decision-making based on learned associations necessarily involves a brain-wide network that links primary sensory areas, the medial temporal lobe, and higher cortical areas involved in executive function. Numerous studies have highlighted the significance of the hippocampus and prefrontal cortex (PFC) in cognitive processing related to memory and decision making[15-19]. Both regions are known to encode behaviorally relevant cues and task features[2-4,20-22], and have been shown to play key roles in memory recall[23-26]. Notably, coordinated activity between the hippocampus and PFC, supported by bidirectional anatomical connections[27-29], has been shown to be critical for learning and memory-guided behavior[30-35]. Therefore, we focused on the coordinated interactions between hippocampus and PFC as a potential key mechanism through which learned associations are recalled and translated into memory-guided decisions.

Several studies have shown that rhythmic network oscillations in the local field potential (LFP) are involved in long-range interactions between the hippocampus and PFC[30,36-40]. In particular, phase coherence in distinct frequency bands across this network has been suggested as a mechanism for network coordination underlying mnemonic functions. Notably, hippocampal-prefrontal coherence in the theta rhythm (6-12 Hz) plays a role in spatial working memory and acquisition of spatial tasks[37,38,41,42]. However, whether similar mechanisms of

coordination between hippocampus and PFC underlie decision making based on sensory cued associations is unclear.

Rodents rely heavily on odor cues for navigation and foraging, so odor memories are highly salient and robust[43-46], making olfactory memory tasks ideally suited for studying memory-guided decision making. Previous studies using odor memory tasks have found prominent beta (15-30 Hz) oscillations in olfactory regions and the medial temporal lobe during cue sampling, suggesting that the beta rhythm acts as a potential mode of long-range communication for olfactory information processing[5,47-50]. In addition to the beta rhythm, the respiratory rhythm (RR; 7-8 Hz), driven by the animal's breathing cycle, is also prominent in the hippocampus during mnemonic processing of odor stimuli[51-55]. However, not much is known about the roles of these rhythms in coordinating activity in the hippocampal-prefrontal network during odor-cued decision making.

To elucidate these mechanisms, we employed an odor-place association task in which rats were required to choose the correct trajectory on a T-maze by recalling and utilizing familiar associations between odor cues and reward locations. While rats were performing the task, we recorded simultaneously from the hippocampus and PFC. Given the involvement of both of these regions in odor-memory tasks[34,56-62], and the role of hippocampal-prefrontal networks in memory-guided behavior[23,24,26,63-65], we hypothesized that rhythmic activity in this network may govern the cellular representation of odor-cued decisions underlying behavioral choices. We also monitored LFP activity in the olfactory bulb (OB) in addition to CA1 and PFC, for robust samplings of previously reported olfactory rhythms such as beta and RR, which have been implicated in cognitive processing of olfactory stimuli[66,67]. Our results point to a specific role of beta rhythms in coordinating the olfactory-hippocampal-prefrontal network for utilizing learned odor-place associations to inform decisions, and shed light on the cellular and network mechanisms underlying this process.

RESULTS

Odor-place associative memory and decision-making task

The odor-cued spatial associative memory task required rats to sniff at an odor port where one of two possible odors was presented using a calibrated olfactometer (see **Methods**). The rats were required to choose the correct associated reward arm on the T-maze based on the sampled odor identity, where they would receive a reward of evaporated milk (**Fig. 1a**).

Rats were habituated to the maze and pre-trained on the task before surgical implant of a tetrode microdrive array for recording neural data. Following post-operative recovery and during electrophysiological recording, animals maintained a high level of performance on the task, indicating accurate decision making based on cued recall of odor-place associations (**Fig. 1b**, n = 8 rats, 77.0% ± 1.3%, mean ± s.e.m.). Rats were required to hold their nose in the odor port for a minimum of 0.50 seconds on each trial, but could continue sniffing the odor for any length of time after the minimum threshold was reached. The odor was continuously dispensed for the entire duration of time that the rat held its nose in the odor port and was only turned off once the rat disengaged from the odor-port. The average odor-sampling duration before odor port disengagement and odor offset was 0.82 ± 0.02 seconds (mean ± s.e.m. across sessions), and this duration was similar between correct and incorrect trials (**Fig. 1c**; signed-rank test, p = 0.71, distribution for all trials shown in **Supplementary Fig. 1a**). The animals' average velocity during the task showed a decrease in speed from the pre-odor period to the odor sampling period in the odor port, followed by an increase in speed after they left the odor port to run to the reward location (**Supplementary Fig. 1b-c**). We observed rapid movement away from the odor-port only after odor-port disengagement (**Supplementary Fig. 1d**). In two animals, a thermocouple was implanted in the nasal cavity to measure the sniff rhythm (see **Methods**). There was a small but significant increase in sniff rate during the odor sampling period (7.1 ±

93 0.39 Hz, mean ± s.e.m.) compared to time matched pre-odor periods (6.2 ± 0.29 Hz, mean ±
94 s.e.m.) (**Supplementary Fig. 1e**).

95 Notably, we observed that on a majority of trials (95.4% ± 0.12%), the animals' turn
96 direction away from the odor port matched the direction of the T-maze reward arm that they
97 would ultimately choose on that trial. This behavioral phenomenon was not required for
98 successful performance of the task, and it occurred regardless of whether the trial was correct
99 or incorrect (**Fig. 1d**; binomial tests, correct trials: $p = 0$; incorrect trials: p = 1.4e-108). This
100 observation indicates that the rats recall the odor-place association and choose the reward
101 location for each trial *during* the odor sampling period, before exiting the odor port to run toward
102 reward. The time of disengagement from the odor port thus provides a trial-by-trial estimate of
103 the moment at which the animal executes the decision. The odor sampling period corresponds
104 to odor-cued recall of the learned association and priming of the subsequent decision to turn
105 toward the reward location, with behavioral report of the decision occurring at odor port offset.
106 We therefore termed this odor sampling period as "the decision-making period," since it
107 provides a temporal window between odor onset and odor port exit to investigate mechanisms
108 underlying odor-cued decision making.

109

110 **Beta rhythms support decision making based on odor-place associations**

111 We therefore focused on the decision-making period and first sought to determine the
112 network dynamics that underlie coordination of brain regions during this period. We used a
113 tetrode microdrive array to record local field potentials (LFPs) and single units from the dorsal
114 CA1 region of the hippocampus, the prelimbic region of the prefrontal cortex (PFC, primarily
115 prelimbic area), and the olfactory bulb (OB, only LFP) in rats as they performed the odor-place
116 association task (see **Methods**; **Supplementary Fig. 2a-b**). The thermocouple signal and LFP

117 traces from CA1, PFC, and OB from an example trial are shown in **Fig. 2a**, along with the same
118 LFP signals filtered in the 15-30 Hz band (additional example shown in **Supplementary Fig.**
119 **2c**).

120 We observed a strong increase in power in the beta band (15-30 Hz) during this
121 decision-making period compared to a time-matched pre-odor period across all three regions
122 (**Fig. 2b**; **Supplementary Fig. 2d-e**). Similar increases in beta power during odor discrimination
123 tasks have been reported previously in OB, CA1, and lateral entorhinal cortex[5,47-49]. The
124 respiratory rhythm (RR, 7-8 Hz) was also prominent in the LFP in all three regions[51,53], showing
125 an increase in power in PFC and OB during odor-sampling compared to time-matched pre-odor
126 periods (**Fig. 2b; Supplementary Fig. 2d,f**). This rhythm, which corresponds to the respiration
127 rate during odor sampling, has previously been shown to be physiologically and mechanistically
128 distinct from the 6-12 Hz hippocampal theta rhythm[51,53], although there is overlap between the
129 two frequency bands. Following odor port disengagement and the initiation of running down the
130 track, we observed a small shift in the dominant LFP frequency from RR to the theta band in
131 CA1 and PFC, reflecting the change in behavioral state (**Supplementary Fig. 2g**).

132 During the decision-making period, we found phase-amplitude coupling between beta
133 and RR in all three regions, consistent with previous findings[53] (**Supplementary Fig. 2h),** and
134 suggesting a mechanistic relationship between the two rhythms. Despite this relationship,
135 previous literature shows that the two rhythms are differentially generated and maintained in the
136 olfactory system and hippocampus and appear to serve different functions in olfactory
137 processing[66-69]. This indicates that the beta rhythm is not merely a harmonic of RR despite
138 apparently similar modulations in amplitude during this task.

139 Odor sampling during the decision-making period thus drives prominent increases in the
140 beta and RR rhythms in OB, CA1 and PFC. We next examined LFP coherence and its temporal
141 dynamics in relationship to behavior. The hippocampal-prefrontal (CA1-PFC) network exhibited

142 prominent and consistent coherence at the beta frequency band during odor sampling, prior to
143 the decision execution at odor-port offset (**Fig. 2c**). This coherence was specific to the odor-
144 sampling period: it significantly increased compared to time-matched pre-odor periods (**Fig. 2d,**
145 sign-rank test, p = 6.7e-6), and diminished shortly after the rat exited the odor port, once the
146 decision had been made (**Fig. 2c**). Additionally, we observed coherence in the RR band in the
147 CA1-PFC circuit, although there was no significant change between pre-odor and odor-sampling
148 periods (**Fig. 2d,** signed-rank test, p = 0.36). During running, after the decision-making period,
149 the prominent low frequency RR coherence shifted to be slightly higher and centered on the
150 canonical theta band (6-12 Hz), similar to what was observed in the LFP power spectrum
151 (**Supplementary Fig. 3a**). Beta and RR coherence were also observed between the CA1-OB
152 and PFC-OB regions during odor sampling periods, with similar temporal dynamics as CA1-PFC
153 beta coherence (**Supplementary Fig. 3b-c**).

154 To directly examine the influence of rhythmic coordination on task dynamics, we asked
155 whether the animal's decision latency, indicated by odor port exit time, was linked to the degree
156 of network coordination. A significant negative correlation between the decision latency time and
157 CA1-PFC beta coherence indicated that a higher degree of beta coordination in the network is
158 associated with faster decisions, whereas there was no significant correlation between RR
159 coherence and decision latency time (**Fig. 2e,** beta: r = -0.54, p = 4.4e-4; RR: r = 0.03, p =
160 0.87). Similarly, CA1-OB beta coherence, but not RR coherence, was also correlated with
161 decision latency (**Supplementary Fig. 3d**), but there was no significant relationship between
162 decision latency and PFC-OB coherence in either frequency band (**Supplementary Fig. 3e**).

163 To control for the possibility that elevated beta coherence during the decision-making
164 period was simply a reflection of passive movement preparation, as has been observed in
165 sensorimotor cortex[70,71], we compared CA1-PFC beta coherence during the last 500ms of the
166 decision-making period with the 500ms just prior to reward well exit. We confirmed that beta

coherence observed during the decision-making period was significantly higher than coherence at the reward well. **(Fig. 2f,** signed-rank test, p = 1.2e-7). In an additional control, we also confirmed that this elevated beta coherence was specifically seen during odor-cued decision making and was not present in sessions in which only air was presented at the odor-port (see **Methods**). In these air-only sessions, reward was given on random trials at the reward locations, even though no odors were presented. RR coherence was unchanged between odor- and air-cued sessions, but beta coherence was significantly lower during air-cued sessions (**Supplementary Fig. 3f-g**).

Although we found a strong relationship between beta coherence in the CA1-PFC network and decision latency, we did not find a direct relationship between the strength of beta coherence or RR coherence to correct performance on the task. There was no significant change in the level of coherence in the CA1-PFC network in either frequency band between correct and incorrect trials (**Fig. 2g,** signed-rank tests; beta: p = 0.38; RR: p = 0.81). This pattern was true of CA1-OB coherence (**Supplementary Fig. 3h**), as well as PFC-OB coherence (**Supplementary Fig. 3i**). Additionally, although beta power was higher on correct trials compared to incorrect trials in PFC, this was not true of either CA1 or OB (**Fig. 2h** (top row), signed rank test; CA1: p = 0.08; PFC: p = 9.3e-4; **Supplementary 3j**). RR power was unchanged between correct and incorrect trials in all three regions (**Fig. 2h** (bottom row), bootstrap test; CA1: p = 0.26; PFC: p = 0.16; **Supplementary 3j**). Therefore, while beta coherence in the CA1-PFC network may facilitate quicker decision making, the strength of oscillatory coordination in the network may not directly or inherently enable a correct decision suggesting that oscillatory modulation of cellular activity may instead play a role.

We were curious if these beta rhythm dynamics were limited to the odor sampling location on the maze. Indeed, CA1-PFC network beta power and coherence were clearly isolated to the region near the odor port (**Fig. 2i**). Finally, since hippocampal sharp-wave ripples

192 (SWRs) have been proposed as a mechanism for memory retrieval, decision making, and
193 planning in some tasks[13,72-74], we also investigated the occurrence of SWRs during our task.
194 SWR events occurred frequently at the two reward locations, as expected[75]. However, a distinct
195 lack of SWR events at the odor port (**Figs. 2i** and **2j**; signed-rank test, p = 1.1e-7) suggests that
196 SWR replay is unlikely to play a direct role in decision making based on recalled associative
197 memories for this well-learned task; rather, the beta rhythm appears to be a primary
198 coordination mechanism for this function. Together, these results suggest that the beta rhythm
199 specifically plays a principal role in odor-cued decision making in this task, while RR may play a
200 more passive role in organizing sensory information transfer during cue utilization.

201

202 **Single neurons in CA1 and PFC exhibit choice selectivity during decision-making period**

203 In addition to LFP, we recorded single units from hippocampal CA1 (n = 1,309 units) and
204 PFC (n = 717 units) (distribution of neurons across animals shown in **Supplementary Table 1**).
205 Units that were active during run sessions were categorized into pyramidal cells and
206 interneurons based on firing rate and spike width (see **Methods,** CA1: 87% pyramidal, 13%
207 interneurons; PFC: 87% pyramidal, 13% interneurons). Pyramidal cells were then further
208 categorized as task-responsive or task-unresponsive based on whether they exhibited
209 significant changes in firing rate during odor sampling (see **Methods**; n = 125 task-responsive
210 CA1 cells, n = 157 task-responsive PFC cells). We observed an overall increase in spiking
211 during the odor sampling period in the task-responsive cell population, suggesting that the
212 majority of these cells increase their firing rate during this period (**Supplementary Fig. 4a**).
213 Interestingly, however, there was an overall decrease in spiking in the average peri-stimulus
214 time histograms when pooling all spikes from all cells during the odor-sampling period
215 (**Supplementary Fig. 4b**), suggesting a decrease in overall responsiveness in CA1 and PFC

networks during odor sampling. Additionally, we confirmed that task responsive neurons were not simply modulated by the animals' decrease in speed at the odor-port by comparing firing rates during odor sampling to firing rates during reward consumption, when speed was also low. We found task-responsive cells' firing rates were significantly higher at the odor port than at the reward wells (**Supplementary Fig. 4c**).

A subset of task-responsive cells was selective for specific choices, based on the identity of the odor and the associated choice. Selectivity was calculated by generating a selectivity index (SI), in which the difference between the average firing rate response to each odor on correct trials was divided by the sum of the two responses, giving a value between -1 and 1 (see **Methods**). To determine significance, the SI value for each cell was compared to a distribution of SIs generated by shuffling the odor identities across trials (n = 42 CA1 selective cells, n = 49 PFC selective cells) (**Figs. 3a** and **3f**). Although the number of selective cells that we observed was relatively low, these numbers were consistent with other studies examining single unit responses to odor stimuli in these regions[8,76,77].

Peri-stimulus time histograms and raster plots aligned to decision time for two example selective cells for CA1 and PFC are shown in **Figs. 3b** and **3g** respectively. Notably, we found that on incorrect trials, selective cells often exhibited responses to the two odors that were opposite to the responses on correct trials. (Examples shown in **Figs. 3c** and **3h**). We found that this phenomenon held true across the population of selective cells, such that overall, the SIs on correct trials were anti-correlated with the SIs on incorrect trials (**Figs. 3d-e** and **3i-j).** Note that since there are only two possible choices on the task, the behavioral response on an incorrect trial is identical to that of a correct trial of the opposite odor. The fact that the neural responses on trials with identical behavioral responses are similar indicates that selective cells are not simply coding the odor identity but are instead responsive to the animal's memory-guided decision and upcoming behavioral choice. In contrast, selectivity to the odor identity

241 alone would result in similar responses to a given odor regardless of the upcoming behavior or
242 the ultimate trial outcome. We therefore termed these cells choice-selective cells. This pattern
243 did not persist within the population of neurons that were task-responsive but did not meet the
244 selectivity threshold (**Supplementary Fig. 4d-e**). Histograms showing distribution of absolute
245 selectivity indices between selective and nonselective cells are shown in **Supplementary 4f.**

246 Putative interneurons were also divided into task-responsive and task-unresponsive,
247 using the same criteria as for putative pyramidal cells (**Supplementary Fig. 4g**).
248 **Supplementary Fig. 4h-i** shows interneuron odor selectivity indices and response properties.
249 For CA1 interneurons, the selectivity response was similar to that of pyramidal cells. PFC
250 interneurons' SIs on correct and incorrect trials were not anti-correlated, although there were
251 very few selective PFC interneurons overall.

252

253 **Neural ensemble responses during decision making are governed by beta coordination**
254 **and predict the upcoming choice**

255 We next examined how ensemble dynamics underlie the neural representation of
256 decisions informed by odor-cued recall. We considered all cells that were task-responsive
257 (regardless of the significance of SI for individual cells) for the ensemble analyses. For the
258 population of task-responsive cells, we found that the distribution of the peak response times in
259 both CA1 and PFC tiled the entire decision time window (**Fig. 4a**). Using the population
260 differential index (PDI) as a measure of population response discriminability (see **Methods**), as
261 described previously[5], we found that distinct representations for the two possible choices
262 emerged gradually in the neural population during the decision-making time period (**Fig. 4b**).
263 Briefly, for this analysis, all task-responsive cells were pooled across animals and days into a
264 single population. Mean firing rates were calculated in 100ms bins to obtain population vectors

265 (PVs) for each of the two odors, and at each time bin the correlation coefficient between the two
266 PVs was calculated. This correlation coefficient was subtracted from 1 to obtain the PDI, such
267 that PDI = 1 indicates that the population responses for the two odors are completely distinct,
268 whereas PDI = 0 indicates that the responses are identical. Chance-level PDI was computed by
269 shuffling the odor identities across trials and creating a null distribution.

270 To determine when this discriminability emerged in the CA1 or PFC ensembles, we
271 performed a bootstrap test, in which a subset of 50 neurons from each region was randomly
272 sampled with replacement to use for the PDI calculation. The timepoint at which the population
273 responses to the odors were considered significantly distinct from each other was defined as the
274 first timepoint at which the real PDI surpassed the 95% confidence interval of the null (shuffled)
275 distribution. This procedure was repeated 500 times to generate a distribution of discrimination
276 times for each region, aligned to odor port disengagement. These bootstrapped distributions
277 were compared, which suggested that discriminability in the CA1 and PFC ensembles emerged
278 simultaneously (**Fig. 4c,** CA1: median = 0.19 seconds prior to odor-port disengagement,
279 interquartile range = 0.06; PFC: median = 0.23 seconds prior to odor-port disengagement,
280 interquartile range = 0.06; bootstrap test, p = 0.31).

281 We were next interested in whether the timing of neural discrimination for CA1 and PFC
282 ensembles on each trial (determined as the time of peak PDI discrimination value) was related
283 to the decision latency. We determined the timing of peak PV discrimination in each region on
284 individual trials by comparing the task-responsive PVs on each trial to the average PV on trials
285 with the opposite odor. Trials in which fewer than 3 total task-responsive neurons in the region
286 were active were excluded, since at least three datapoints are needed to calculate a meaningful
287 correlation between PVs. On individual trials, the timing of peak discrimination for both CA1 and
288 PFC ensembles had small but significant correlations with the decision latency (**Fig. 4d,** CA1: n
289 = 2241 trials, r = 0.09, p = 4.1e-5; PFC: n = 2087 trials, r = 0.06, p = 0.01; individual trial rasters

shown in **Supplementary Fig. 4j**). This implies a temporal link between the emergence of the decision in the CA1 and PFC neural populations, and the moment when the animal begins to execute a behavioral response.

We next asked whether the timing of this neural ensemble discriminability between the two choices was related to beta coordination in the network on each trial. Indeed, we found that the timing of peak CA1 PV discriminability on individual trials was weakly but significantly anti-correlated with the strength of CA1-PFC beta coherence, such that high CA1-PFC coherence trials had an earlier PV divergence latency and therefore earlier neural discrimination; however, no significant correlation was seen for PFC PV divergence time. (**Fig. 4e**, CA1: $r = -0.12$, $p = 2.1e-8$; PFC: $r = -0.03$, $p = 0.09$). Furthermore, we found that the timing of peak beta coherence on each trial was also weakly but significantly correlated with the timing of peak PV discriminability, in both CA1 and PFC (**Supplementary Fig. 4k**, CA1: $r = 0.05$, $p = 0.02$, PFC: $r = 0.04$, $p = 0.04$), further suggesting a temporal relationship between beta coherence in the CA1-PFC network and coding of the choice by neural ensembles.

To determine whether the animal's upcoming behavior could indeed be predicted by neural ensembles before the decision was executed, we trained a generalized linear model (GLM) to predict the animal's choice based on ensemble activity during the decision-making period (See **Methods**). We performed this analysis using task-responsive putative pyramidal cells and found that reward choice could be accurately predicted 0.1 seconds prior to odor port disengagement by CA1 ensembles, and 0.3 seconds prior by PFC ensembles (**Fig. 4f**). Additionally, we performed the same analysis, but included both task-responsive pyramidal and interneurons in the ensembles. In this case, we found an improvement in prediction for CA1 ensembles: reward prediction was now accurate starting earlier, at 0.2 seconds prior to decision execution. Prediction by PFC ensembles remained the same. (**Fig. 4g**). To control for the possibility that inclusion of interneurons improved prediction latency for CA1 simply due to the

315 larger number of cells in the training set, we performed this analysis again by resampling the
316 pyramidal cells to match the total number of pyramidal cells plus interneurons used in **Fig. 4g.**
317 In this control analysis, we found that the choice could again only be predicted at 0.1 seconds
318 prior to the decision execution, the same as what we observed with the original sample of
319 pyramidal cells. These results confirm that the animals utilize the recalled odor-place
320 association and make a spatial choice during this odor-sampling period, which is reflected in the
321 activity of task-responsive neural ensembles. Further, beta coordination in the CA1-PFC
322 network is linked to the neural activity dynamics underlying this memory-guided decision
323 process.

324 To investigate whether there was evidence of coordination between ensembles in CA1
325 and PFC, we wanted to determine whether the spiking of neuronal ensembles in the two regions
326 were temporally linked[78,79]. In order do this, we computed the Z-scored cross-correlation for all
327 CA1-PFC pairs of task-responsive neurons (**Fig. 4h**). Interestingly, we found that the distribution
328 of the peaks of the cross-correlations for pairs of putative pyramidal cells (n = 603 pairs) was
329 bimodal, with a peak at -28.5ms and another at 13.3ms. This points to potential bi-directional
330 spike-time coordination between the pyramidal ensembles in the two regions. Since we also
331 found task-responsive interneurons that contributed to prediction of upcoming choice, we
332 hypothesized that inter-regional coordination may also be shaped by interneuron activity. To
333 examine temporal relationships between interneurons, we performed the same cross-correlation
334 procedure for all CA1-PFC pairs of task-responsive interneurons (n = 85 pairs), as well as pairs
335 of CA1 interneurons and PFC pyramidal cells (n = 462 pairs), and vice versa (n = 130 pairs).
336 We found a prominent peak at 0ms for CA1-PFC interneuron pairs, as well as CA1 pyramidal
337 cell - PFC interneuron pairs. Additionally, we found a significant 9.5ms lag in the CA1
338 interneuron- PFC pyramidal cell cross-correlation peak distribution. These results suggest
339 temporal relationships between these populations, and especially that CA1 interneuron activity

may have a role in sculpting PFC task-responsive ensembles, further suggesting coordination between the two regions during cue-processing and decision-making.

CA1 and PFC cells phase lock to beta and respiratory rhythms during decision making

We next asked if there was any relationship between oscillatory phase modulation of cells and decision accuracy. Within the population of task-responsive cells in both CA1 and PFC we found a fraction of cells that were phase locked to the beta rhythm during the decision-making period (see **Methods**; CA1: n = 36, 28.8%; PFC: n = 17, 10.8%). Spike-phase histograms for two example beta-phase locked cells are shown in **Fig. 5a** (Rayleigh Z test, CA1: n = 242 spikes, z = 15.4, p = 1.5e-7; PFC: n = 99 spikes, z = 4.9, p = 0.007). We also found that many cells in the task-responsive populations were strongly phase locked to RR (CA1: n = 112, 89.6%; PFC: n = 60, 38.2%). Examples for two of these cells are shown in **Supplementary Fig. 5a**. For both beta and RR, there was a significant non-uniformity in beta phase-preference across cells in CA1, and nonuniformity in only beta-phase preference for PFC populations (**Fig. 5b**, Rayleigh Z test; CA1: z =7.88, p = 3.4e-4; PFC: z = 4.9, p = 0.007. **Supplementary Fig. 5b**). The preferred phases of the two cell populations were distinct for both regions (**Fig. 5b,** Watson-Williams test, $p < 0.001$, **Supplementary Fig. 5b**).

Since our results so far suggested that the beta rhythm may have more relevance to decision latency and ensemble coordination than RR, we next asked whether phase locking to the beta rhythm was indicative of accurate decision making. To do this, we compared Rayleigh Z scores, a measure of non-uniformity in the spike-phase distribution, on correct versus incorrect trials for significantly phase-locked cells. For each phase-locked cell, we calculated the Rayleigh Z score for the spike-phase distribution on correct trials for incorrect trials separately and compared these two paired distributions. We found that in both CA1 and PFC, cells that

364 were phase-locked to the local beta rhythm exhibited a lower Rayleigh Z on incorrect trials.
365 There was no significant effect for cross-regional modulation however (**Fig. 5c**, signed-rank
366 tests, CA1-CA1: n = 28, p = 0.03; PFC-PFC: n = 8, p = 0.007; CA1-PFC: n = 18, p = 0.39; PFC-
367 CA1: n = 12, p = 0.20). This suggests that local spiking modulation by the beta rhythm in CA1
368 and PFC can potentially play a role in supporting accurate utilization of odor-place associations
369 for making decisions. CA1 cells that were phase-locked by local CA1 RR also showed a slight
370 but significant decrease in modulation on incorrect trials, but we found no change in modulation
371 strength for locally phase locked PFC cells, nor for cross regional RR phase modulation in either
372 population between correct and incorrect trials (**Fig. 5d**, signed-rank tests, CA1-CA1: n = 103
373 cells, p = 0.04; PFC-PFC: n = 35 cells, p = 0.38; CA1-PFC: n = 85 cells, p = 0.26; PFC-CA1: n =
374 49 cells, p = 0.30). Note that the LFP and spiking analyses found stronger evidence that beta
375 coordination is related to task performance (**Figs. 2, 4, 5c**), even though a higher percentage of
376 cells in both regions were phase locked to RR (**Fig. 5e**, z-test for proportions, CA1: p = 6.8e-23;
377 PFC: p = 8.8e-9) and this modulation was much stronger for RR compared to beta
378 (**Supplementary Fig. 5c**). Additionally, in both CA1 and PFC, the proportion of cells that were
379 phase locked to both beta *and* RR was no different than chance, given the percentages of cells
380 that were modulated by either rhythm (**Supplementary Fig. 5d**). This suggests that the two
381 rhythms simultaneously modulate slightly different populations of cells, supporting the
382 interpretation that the two rhythms play separate, though cooperative, roles in memory-guided
383 decision making.

384 Are cells that are modulated by beta the same population of cells that code for the
385 upcoming decision? To test this, we compared the number of pyramidal cells that were both
386 choice-selective *and* phase-locked (within and across regions) to the fraction that would be
387 expected by chance, given the total percentages of cells that are choice-selective or phase-
388 locked. Interestingly, we found that the number of cells that met both criteria was no different

389 than chance for either CA1 or PFC (**Fig. 5f**, binomial tests; CA1: p = 0.097; PFC: p = 0.17). We
390 found similar results for RR modulation (**Supplementary Fig. 5e**). It should be noted that since
391 such a large majority (~90%) of neurons in CA1 were significantly phase locked to RR, it is
392 unsurprising that almost all the choice-selective cells were phase locked to this rhythm.
393 However, this result indicates that the choice-selective cells were no more or less likely than
394 non-selective cells to phase lock to RR. Together, these results suggest that, surprisingly, the
395 putative pyramidal neural ensembles that code for the primary task parameter of odor-cued
396 associative decisions may not be driven directly by the beta rhythm, with relatively low
397 prevalence of beta phase modulation, despite the strong relationship we observed between beta
398 oscillations, choice-selective ensemble activity and memory-guided decision latency (**Figs. 2,**
399 **4**).

400 We therefore examined the role of beta oscillations in coordinating the activity of
401 interneurons in the CA1-PFC network. Indeed, we found high prevalence of beta phase
402 modulation of CA1 interneurons. Of the 102 interneurons in CA1 that were active during the
403 decision period, 44 (43.1%) were phase-locked to the local CA1 beta rhythm, and 25 (24.5%)
404 were phase-locked cross-regionally to the PFC beta rhythm. Phase preference among the
405 neurons in both groups was strongly non-uniform and unimodal (**Fig. 5g**), indicating local- and
406 cross-regional coordination of CA1 interneurons is governed by beta in a strongly phase-
407 dependent manner. In contrast, very few of the 37 PFC interneurons were phase-locked to beta,
408 both locally (3 units, 8.1%) and cross-regionally (1 unit, 2.7%).

409 Local and cross-regional beta phase modulation of CA1 interneurons was lower on
410 incorrect compared to correct trials (**Fig. 5h,** signed-rank tests, CA1-CA1: p = 8.2e-9; CA1-PFC:
411 p = 1.2e-5), suggesting that entrainment of CA1 interneurons to the network-wide beta rhythm is
412 linked to task performance. About half of the CA1 interneurons that were choice-selective were
413 also beta phase-locked, although this number was not different than what would be expected by

414 chance (**Fig. 5i,** binomial tests; CA1: p = 0.11; PFC: p = 0.20), similar to what we observed in
415 the population of putative pyramidal cells. Our results suggest, therefore, that CA1 interneuron
416 activity is strongly governed by the beta rhythm locally, as well as in a coordinated manner with
417 PFC. This also aligns with the finding of temporal relationships in cross-correlations between
418 CA1 interneurons and PFC pyramidal cells and interneurons (**Fig. 4h**). Beta modulation of
419 interneurons may thus constrain and coordinate network activity, and may play a role in
420 sculpting pyramidal cell ensembles in local circuits to enable processing of odor-cued
421 associations for translation to decisions.

422

423 **Representations of choice and space are maintained independently during delay period**

424 Finally, we investigated if there was any relationship between the activity of CA1 and
425 PFC ensembles during the odor-cued decision-making period and their spatial activity on the
426 maze as the animals ran through the delay period on the central and side arms toward reward.
427 We examined units from sessions in which animals traversed a long T-maze track (see
428 **Methods**, 26 sessions from 6 rats) in order to assess spatial firing characteristics. A large
429 fraction of cells in CA1 and PFC exhibited spatial activity on the maze (see **Methods** for details
430 on spatial parameters, n = 344 out of 585 CA1 cells; n = 159 out of 288 PFC cells had fields on
431 the track), including units that were both task-responsive (choice selective and non-selective)
432 and task-unresponsive (**Figs. 6a, 6b**; examples of CA1 and PFC choice-selective cells with
433 spatial fields in **Fig. 6a,** examples of CA1 and PFC task-responsive but non-selective cells with
434 spatial fields shown in **Supplementary Fig. 6a**).

435 Cells that were task-responsive were more likely to have spatial fields on the track (odor
436 sampling periods were excluded in spatial responses, see **Methods**), compared to cells that
437 were not responsive during the odor sampling period (**Fig. 6b**, binomial test, CA1: p=0.029;

438 PFC: p=2.7e-5). Additionally, for both CA1 and PFC neurons, we found that the firing rate
439 during odor sampling was correlated with firing rate during running (**Fig. 6c,** CA1: r = 0.39, p =
440 3.0e-37; PFC: r = 0.68, p = 1.2e-62), and task-responsive cells had higher firing rates overall
441 (**Supplementary Fig. 6b**), suggesting a possible relationship between cell activity during
442 decision making and maintenance of the decision during the spatial delay. To examine this
443 question further, we asked whether the spatial fields in either CA1 or PFC exhibited different
444 characteristics based on whether they were responsive during the decision-making period.
445 Surprisingly however, we found no difference in field width (**Fig. 6d,** rank-sum tests, CA1: p =
446 0.15; PFC: p = 0.92), field peak rate (**Supplementary Fig. 6c**), or field sparsity
447 (**Supplementary Fig. 6d**) between cells that were task-responsive and task-unresponsive in
448 either region.

449 Further, we also examined trajectory selectivity as animals ran through the central arm
450 and on the side arms toward reward (examples of trajectory selective firing shown in **Fig. 6a,**
451 second row). Trajectory selectivity was defined by comparing spatial tuning curves of cells on
452 right versus left trajectories and calculating a selectivity index analogous to the choice selectivity
453 index during the decision-making period (see **Methods**). Interestingly, although trajectory-
454 selective cells were significantly more likely than trajectory-nonselective cells to respond in the
455 decision-making period (**Supplementary Fig. 6e**), there was no relationship between the
456 preferred trajectory during run periods and preferred choice during the odor-cued decision-
457 making period (**Fig. 6e,** rank sum test CA1: p = 0.26; PFC: p = 0.20)**.** Thus, although CA1 and
458 PFC cells that were task responsive had higher firing rates and therefore higher engagement
459 while traversing trajectories on the maze, there was no clear relationship between choice
460 selectivity and trajectory selectivity in either CA1 or PFC.

461 To confirm this result, we sought to determine whether choice selective neuronal activity
462 in the population during decision making persisted into the following run period. To examine

463 this, the linearized T-maze was divided into 5 equally spaced quintiles and a Bayesian Classifier
464 trained on odor period activity was used to decode the choice identity from the ensemble activity
465 during run at each spatial quintile (see **Methods**; similar results were seen for spatial quartiles).
466 We found that choice identity could be decoded at the first quintile of track, nearest to the odor
467 port, but decoding accuracy diminished to chance level thereafter (**Fig. 6g**). In contrast, the
468 animal's upcoming behavioral choice could be accurately decoded at all periods along the
469 trajectory if instead the spatially active ensembles in each respective spatial quintile was used
470 as the training set (**Fig. 6h**). This suggests that the choice selectivity that emerges in ensembles
471 during odor sampling (**Fig. 4**) persists transiently for a short period past the decision point, but
472 that separate ensembles maintain choice-related information as animals traverse the spatial
473 trajectory, possibly corresponding to theta oscillations during run (**Supplementary 2g**). This is
474 further supported by the fact that, at least for CA1, choice-selective ensemble firing rate is
475 highest within 20 cm of the odor port, and decreases thereafter (**Supplementary Fig. 6f**).These
476 results together suggest that the choice-selective ensembles reflecting decision making during
477 the odor-cue period transiently encode the choice during the initial track period, but the decision
478 is subsequently maintained by a distinct ensemble during the working-memory period
479 associated with the spatial delay on the central arm.

480

481 **DISCUSSION**

482 Our results provide new insight into the mechanisms of rhythmic coordination of
483 hippocampal–prefrontal ensembles by beta rhythms for odor-cued associations and decision
484 making. We found that during an odor-place associative memory task, beta rhythms govern
485 physiological coordination between the olfactory bulb, hippocampus, and PFC. During the odor
486 sampling and decision-making period, task-responsive single unit and ensemble activity in the
487 CA1-PFC network discriminates between choices and can reliably predict upcoming behavior.

488 Further, CA1-PFC ensemble dynamics and beta coherence during this period are linked to
489 latency of decisions. Despite this link, we did not find evidence for direct beta phase modulation
490 of choice-encoding putative pyramidal neurons. Instead, we found that interneurons in CA1
491 were strongly locally and cross-regionally phase modulated by beta. This suggests that
492 coordination by beta rhythms may sculpt network activity through interneuron modulation,
493 enabling emergence of task-related ensemble dynamics in local circuits to support decision
494 making. Our results thus suggest that beta oscillations play a key modulatory role in enabling
495 temporal evolution of ensemble dynamics in the CA1-PFC network for odor-cued decision
496 making, delineating a novel mechanism through which rhythmic coordination supports cognition.

497 The mechanisms underlying encoding and recall of associations between sensory cues in
498 the environment, and subsequent use of these associations to guide decisions, are of
499 fundamental interest. Sensory cue-elicited recall and decision making during goal-directed
500 behavior involves widespread networks encompassing sensory regions, medial temporal
501 memory regions, and prefrontal executive function regions. Prominent odor-driven oscillations
502 have been described in these areas[5,47-53,80], which can potentially coordinate these long-range
503 networks to enable utilization of familiar olfactory cues to guide behavior. Here, the use of an
504 odor-cued T-maze task allowed us to examine which rhythms enable coordination of olfactory-
505 hippocampal-prefrontal networks, and whether these rhythms play a role in patterning ensemble
506 activity in hippocampal-prefrontal network to enable memory-guided decision making.

507 In this task, the time period between odor onset and odor port disengagement provided a
508 temporal window corresponding to odor-cued recall and priming of the subsequent decision to
509 turn toward the reward location. We found increases in power and coherence of both beta (~15-
510 30 Hz) and RR (~7-8 Hz) across the olfactory-hippocampal-prefrontal network during this odor
511 sampling and decision-making period. However, only the strength of beta coherence, and not
512 RR coherence, between the hippocampus and PFC was correlated with shorter decision

513 latency. Further, while CA1-PFC RR coherence remained unchanged between odor-cued trials
514 and trials where only air was presented, high beta coherence was specific to odor-cued trials
515 corresponding to a decision-making task and was lower on air-cued trials corresponding to
516 random choices. Based on these findings, we speculate that encountering a familiar odor
517 stimulus and efficiently utilizing this associative memory for a decision, rather than respiration or
518 movement preparation[81], elicits the engagement of the hippocampal-prefrontal network by the
519 beta rhythm.

520 Interestingly, although hippocampal SWRs have been linked to internal recall and
521 planning[72,73,82], there was very low prevalence of hippocampal SWRs during odor sampling,
522 suggesting SWRs are not directly involved in odor-cued associative memory and decision
523 making while the animal is re-encountering the familiar cue. Instead, our results indicate that
524 beta plays a key role in mediating this process, in addition to coordinating entorhinal-
525 hippocampal networks for odor-cued recall, as described previously[5]. In our experiments, rats
526 were very familiar with the task and odor-place associations, with high performance levels.
527 Therefore, the lack of SWRs during the decision-making period could reflect that these
528 memories had been previously consolidated into neocortex during learning, resulting in a shift
529 from largely hippocampal-dependent processing[5] to processing that is more reliant on
530 hippocampal-cortical dialogue via the beta rhythm.

531 Odor-driven gamma rhythms at 40-100 Hz have also been reported in odor-memory
532 tasks[47,66,83], and may play a complementary role with beta oscillations. It has been hypothesized
533 that local olfactory networks may be governed by gamma rhythms for odor processing early in
534 stimulus sampling, before shifting to a beta-dominant network state as downstream regions are
535 engaged[47,84]. Our results corroborate this hypothesis by reinforcing the role of the beta rhythm in
536 long-range coordination with a wider network outside the olfactory system for cognitive
537 processing of odor stimuli. We speculate that sensory modality-specific rhythms may play a

538 general role in cue-driven mnemonic decision making by coordinating sensory and cognitive
539 areas, which can be tested in future studies.

540 Our analysis of single units in the hippocampus and prefrontal cortex revealed a group of
541 cells that were selectively responsive in the odor task period, similar to previous reports in the
542 hippocampus[5,85,86]. However, we found that these selective cells often exhibited "opposite"
543 selectivity on incorrect trials compared to correct trials, indicating that these cells do not respond
544 solely to the perceptual qualities of the odor, in which case the response would be similar on all
545 presentations of a particular odor regardless of the trial outcome. Instead, this response
546 suggests coding of the behavioral choice associated with the odor cue, resembling findings from
547 studies of combined cue modalities and cue-context associations[1,6-8,10,86-88]. Thus, the CA1-PFC
548 neural response during odor sampling corresponds to the decision in response to the odor-place
549 association. Future studies that combine recording from other olfactory regions, such as piriform
550 cortex, together with hippocampus and PFC can potentially unveil how the cue representation
551 evolves from odor perception to the recall-based decision.

552 Task-responsive neural populations exhibited differential activity patterns in response to the
553 two odor-associations during decision making, and the animal's upcoming choice could be
554 predicted from this ensemble activity. Correlation between the timing of ensemble odor
555 discrimination and choice execution indicates that the emergence of the neuronal representation
556 coincides with and potentially primes the cognitive decision. This emergence of neural
557 ensembles that reflect associative memories governing decision making may also be indicative
558 of a physiological mechanism for dynamic reactivation of memory engrams upon re-
559 encountering the familiar odor stimuli[89,90]. We also found evidence that beta rhythms may
560 govern the temporal evolution of CA1-PFC neural ensemble dynamics leading to memory-
561 guided decision making, as demonstrated by the small but significant correlations between the
562 strength of beta coherence, the timing of ensemble discrimination, and the behavioral decision

563 latency. It remains unclear, however, how these neural dynamics and their relationship to the
564 beta rhythm evolve as animals learn new associations. One possibility is that they resemble the
565 dynamics observed in the hippocampal-entorhinal circuit, in which coordination of the network at
566 the beta rhythm and choice-selective neural activity emerge gradually as animals learn the
567 task[5].

568 Similarly, CA1-OB beta coherence is strong during odor memory tasks and is known to
569 increase over the course of learning[58]. Although CA1-OB beta coherence was high during odor
570 sampling in our task, we observed no significant relationship between CA1-OB coherence and
571 task performance. Since previous reports suggest that this coherence is linked to the learning
572 process, it is possible that a more direct relationship between coherence strength and
573 performance would be observed only during learning, but not in this case where the odor
574 association and task are familiar. Choice-coding ensemble dynamics may evolve in parallel with
575 the increase in CA1-OB beta coherence over learning, similar to what has been reported in the
576 hippocampal-entorhinal circuit[5]. This possibility can be investigated by examining network
577 dynamics and ensemble activity across multiple olfactory and cognitive areas during novel odor-
578 place learning or reversal learning.

579 It is also noteworthy that we observed different mechanisms underlying odor-cued decision
580 making versus subsequent maintenance of the representation of the choice during a spatial
581 delay period. Odor-driven beta coherence leads to emergence of ensemble selectivity during
582 the decision-making period, which is predictive of the animal's upcoming choice, but these
583 ensembles maintain their choice-selectivity only transiently after the decision execution as
584 animals embark on the spatial trajectory toward reward. This selective coding is not maintained
585 by the same ensembles during running, but instead other spatially modulated cells in CA1 and
586 PFC maintain choice coding on the track, including the spatial delay period (common central
587 arm on the T-maze) activity. Thus, beta-driven ensembles mediate memory-guided decision

588 making in the hippocampal-prefrontal network, but choice selective activity is then subsequently
589 maintained by theta-driven spatially modulated activity, similar to reports in spatial working
590 memory tasks[77].

591 The temporal evolution of ensemble activity underlying odor-cued decision making, and
592 its relationship to beta oscillations, is reminiscent of temporal coding of odor stimuli mediated by
593 oscillations in the olfactory system[50,52]. Previous findings indicate that spike timing modulation
594 according to the phase of prominent network rhythms can organize task-encoding neural
595 ensembles to support memory guided behavior and decision-making[42,86,91-94]. Interestingly
596 however, we found that although the strength of local beta and RR phase-modulation was linked
597 to correct decisions, putative pyramidal neurons that encoded the choice were no more likely to
598 be phase-locked than chance level. Notably, phase locking was stronger and more prevalent for
599 RR compared to the beta rhythm, even though behavioral decision latency and choice-coding in
600 the underlying ensembles was more linked to beta coherence in the network. Further, we found
601 evidence that slightly different populations of cells are modulated by the two ongoing rhythms
602 during decision making, implying that beta and RR represent two simultaneous modes of
603 rhythmic coordination in the network[49]. This joint modulation of the underlying cell populations,
604 along with our finding of strong cross-frequency coupling between the two rhythms, leads us to
605 the interpretation that beta and RR coordinate the network cooperatively during odor-cued
606 decision making, rather than acting as independent but parallel processes. Previous reports of
607 RR in olfactory processing[51,52,55], along with evidence that multiple rhythms can simultaneously
608 modulate ongoing processes[49,95,96], suggests that RR is the dominant modulator coordinating
609 the sensory element of the task, while beta coordination is key for employing the sensory cued
610 association to make a decision. This interpretation is further supported by our results from un-
611 cued air sessions, which did not involve memory-guided behavior, in which we found a
612 reduction in beta coherence in the network but no change in RR coherence. This suggests that

613 the sensory component of this process is maintained as the animal continues sniffing even in
614 the absence of an explicit cue, whereas beta coordination is only engaged when a familiar cue
615 is utilized for a decision.

616 In contrast to pyramidal cells, we found that a large population of CA1 interneurons were
617 strongly modulated by the beta rhythm locally and cross-regionally and the strength of this
618 modulation was linked to task performance. This suggests that the beta rhythm can function by
619 modulating CA1 interneuron activity, which sculpts ensemble dynamics in the local circuits
620 governing decision making. In this manner, beta oscillations may play a role in establishing
621 communication and organization of activity in sensory and cognitive networks enabling
622 decisions based on cued associations. Thus, oscillatory phase-modulation may be indicative of
623 a general network state that enables coordination.

METHODS

All experimental procedures were approved by the Brandeis University Institutional Animal Care and Usage Committee (IACUC) and conformed to US National Institutes of Health guidelines. Eight male Long-Evans rats (3-6 months, 450-650 g) were used for experiments. Animals were housed individually in a dedicated climate-controlled animal facility on a 12-hour light/dark cycle. All experiments were carried out during light cycle. Upon arrival, animals were provided ad libitum access to food and water and handled regularly to habituate them to human contact.

Behavior Apparatus

An olfactometer (MedAssociates Inc.) was used for dispensing odors. The olfactometer continuously dispensed clean air to the odor port until receiving a signal to open a solenoid valve which caused air to flow through liquid odorants, resulting in odorized air dispensed to the odor port. A vacuum tube attached to the odor port was used to continuously collect any residual odorized air between trials. Infrared beams were used at the odor port and reward wells to determine the precise timing of entry and exit from these areas.

Odor-Place Association Task Training

Once rats reached a minimum threshold weight of 450 g, they were food restricted to no less than 85% of their free-feeding baseline weight. For initial behavioral training, rats were familiarized with the behavior room, the sleep box, running on a raised track to receive evaporated milk reward, and sniffing odors presented in the odor port. Following this habituation, rats were trained to hold their nose in the odor port for a minimum of 500 ms, with

647 an auditory tone indicating when this 500-ms time threshold was reached. However, the rats
648 could continue to sniff the odor for any longer duration of time, and odor would be continuously
649 dispensed until they disengaged from the odor port. Throughout all training and experiments, if
650 the rat exited the odor port before this threshold was reached, no reward was dispensed
651 regardless of the rat's choice and the rat was required to re-initiate the trial. These prematurely
652 terminated trials were excluded from all analyses. For each trial, the odor sampling period was
653 defined as the time from the onset when rat's nose broke the infrared beam to offset when the
654 beam break was terminated, and odor stimulus was stopped.

655 Animals were subsequently trained on the olfactory association. On each trial, one of
656 two possible odors was dispensed at the odor port in a pseudo-random order. Odor 1 (Heptanol
657 – pine/citrus scent) indicated that the rat should go to Reward 1 to receive reward. Odor 2 (ethyl
658 butyrate – strawberry scent) indicated that the rat should choose Reward 2 (**Fig. 1a**). If the rat
659 ultimately made the correct choice, evaporated milk reward would be dispensed at the chosen
660 reward port upon triggering the infrared beam, whereas upon an incorrect choice no reward was
661 dispensed.

662 Associative memory training was shaped in steps. The rats first learned the association
663 between the odors and "right" vs "left" reward locations with reward wells close to the odor port.
664 On subsequent training days, the reward wells were moved further and further away from the
665 odor port, until rats could comfortably perform the task on the full T-maze (81 cm long center
666 stem, and 43cm long reward arms). Two rats were not trained to run on the full T-maze, and
667 instead were just required to perform the association with the reward wells within easy reach on
668 either side of the odor port. For one animal, the maze had a shortened stem (40 cm instead of
669 81 cm), but the reward wells were still at the ends of the T arms. Task performance was
670 calculated as the proportion of correct trials. Rats were trained until they could perform the task
671 with at least 80% accuracy for 3 consecutive days.

672 Once training was complete, animals were once again provided with *ad libitum* access to
673 food until they reached at least 600 g, before undergoing surgery. After surgery but before
674 recording, rats were briefly re-trained on the association until they could again perform the task
675 with at least 80% accuracy. On recording days, animals were allowed to continue performing
676 the task until they reached satiation, about 100-150 trials per day. Task epochs were interleaved
677 by sleep epochs, in which rats spent about 20 minutes in an opaque sleep box, with a sleep
678 epoch as the first and last epoch of each day.

679

680 **Un-Cued Air Sessions**

681 Four of the animals were tested on one session each in which only clean air was
682 dispensed at the odor port, instead of two distinct odors. Reward was available at a randomly
683 chosen reward port on each trial; although, since the trials were un-cued, the animals would
684 often randomly choose the "incorrect" side and no reward was dispensed (**Supplementary**
685 **Figure 3f**). All other aspects of the task were the same as the odor-cued task.

686

687 **Surgical Procedures**

688 Surgical implantation techniques were performed as described previously[31,98]. Animals
689 were implanted with a microdrive array containing 30 independently moveable tetrodes targeting
690 right dorsal hippocampal region CA1 (-3.6 mm AP and +2.2 mm ML, 10-12 tetrodes), right PFC
691 (+3.0 mm AP and +0.7 mm ML10-13 tetrodes), and right olfactory bulb (+7.2 mm AP and +0.8
692 mm ML, 1-4 tetrodes). Post-operative analgesic care was provided for 48 hours after surgery to
693 minimize pain and discomfort. In two of the eight animals used for experiments, a nasal
694 thermocouple was implanted in addition to the microdrive array to record the respiratory rhythm.
695 The thermocouple was placed in the left nostril though a hole drilled in the skull at +7.5 mm

696 anterior to the cribriform suture. The thermocouple wire was secured using dental acrylic and
697 soldered to the same printed circuit board as the tetrodes.

698

699 **Tetrode Recordings**

700 For 1-2 weeks following surgery, tetrodes were gradually lowered to the desired depths.
701 Hippocampal tetrodes were targeted to the pyramidal layer of CA1 using characteristic EEG
702 patterns (sharp wave polarity, theta modulation) and neural firing patterns as previously
703 described[78,97]. The final placement of tetrodes was confirmed in histological preparations using
704 Nissl staining post-mortem. One tetrode in corpus callosum served as hippocampal reference,
705 and another tetrode in overlying cortical regions with no spiking signal served as PFC reference.
706 A ground screw (GND) installed in the skull overlying cerebellum also served as a reference,
707 and LFP was recorded relative to this GND. All spiking activity was recorded relative to the local
708 reference tetrode. Only LFP activity was recorded from olfactory bulb. Electrodes were not
709 moved at least 4 hours before and during the recording day to reduce drift, and were micro-
710 adjusted at the end of each recording day to sample new cell populations.

711 Data were collected using a SpikeGadgets data acquisition system and software
712 (SpikeGadgets LLC). Spike data were sampled at 30 kHz and bandpass filtered between 600
713 Hz and 6 kHz. LFP signals were sampled at 1.5 kHz and bandpass filtered between 0.5 Hz and
714 400 Hz. The animal's position and running speed were recorded with an overhead color CCD
715 camera (30 fps) and tracked by color LEDs affixed to the headstage.

716

717 **Data Analysis and Statistics**

All data analysis was performed in MATLAB using custom code unless otherwise noted. Error bars indicate standard deviation unless otherwise noted. Significance was defined using an alpha of 0.05. Statistical details including tests used, p-values, and n values can be found in figure legends, and are described in-depth below.

Local Field Potential

Trial-averaged spectrograms and coherograms were calculated using multi-taper spectral methods included in the Chronux package for MATLAB (www.chronux.org). To get the beta filtered local field potential (LFP) signal, raw LFP (with respect to GND) was band pass filtered at 15-30 Hz using a zero-phase IIR filter. Amplitude, phase, and envelope magnitude of the signals were obtained using a Hilbert transform. Beta power and coherence were z-scored to the epoch mean. Similarly, the respiratory rhythm signal was obtained by band pass filtering the raw LFP at 7-8 Hz. Due to the overlap between the RR and the theta rhythm (6-12 Hz), to get an accurate measure of RR power and coherence without leakage from the theta rhythm, this signal was z-scored to time-matched periods during immobility while the animal was consuming reward.

Bootstrap Tests

Bootstrap tests for **Supplementary Fig. 3g** were performed when coherence on odor-cued and air-cued trials were compared, to account for the much larger percentage of odor-cued trials. Data points on odor trials were randomly downsampled with replacement to match the number of air trials, and the mean was calculated for this new set of datapoints. This downsampling was done 1000 times, to create a new, bootstrapped distribution of means. The

741 observed mean value for the air trial distribution was compared to the bootstrapped distribution.
742 P-values were calculated by counting the number of values the bootstrapped distribution that
743 were greater than or equal to the observed mean value, and dividing by the total number of re-
744 samples (1000). P-values less than 0.05 were considered statistically significant, and thus
745 rejected the null hypothesis that the two observed distributions had equal means.

746 The bootstrap test for **Fig. 4c** was performed similarly, except that the CA1 and PFC cell
747 ensembles were resampled to create new ensembles of 50 cells each. The timing of PV
748 divergence for each resampled ensemble was calculated as described below (see **Population**
749 **Differential Index** methods). This procedure was repeated for 500 iterations to generate the
750 distributions shown in **Fig. 4c**.

751

752 **Sharp-Wave Ripple Detection**

753 Hippocampal sharp-wave ripples were detected as previously described[31,78,98]. Briefly,
754 the locally referenced LFP signal from CA1 tetrodes was filtered in the ripple band (150-250
755 Hz), and the envelope of the ripple-filtered LFPs was determined using a Hilbert transform.
756 SWR events were detected as contiguous periods when the envelope stayed above 3 SD of the
757 mean on at least one tetrode for at least 15 ms.

758

759 **Cross-frequency Coupling**

760 Phase-amplitude coupling between RR and beta was computed for **Supplementary Fig.**
761 **2g** as previously described[99]. In brief, the phases of RR were divided into 20 degree bins, and
762 the mean amplitude of the beta rhythm at each phase was calculated. The mean amplitudes

were then normalized by dividing each bin by the sum of amplitudes across all bins. The strength of phase-amplitude coupling was determined by comparing the amplitude distribution to a uniform distribution by calculating the modulation index (MI), which is based on the Kullback–Leibler (KL) distance but normalized so that values fall between 0 and 1, where a value of 0 indicates a uniform distribution of beta amplitudes across RR phases. Significance was determined by comparing the calculated MI to a null distribution generated by shuffling the trial number assignments of the RR phase series; this maintains the structure of the underlying rhythm but randomly aligns the beta amplitudes on each trial to each trial sequence RR phases.

Single Unit Analysis

Spike sorting was done semi-automatically using MountainSort[100,101], with manual curation. Only well-isolated units were used for analysis. Putative interneurons and pyramidal cells were classified based on average firing rate and spike width, as described previously[31,98]. Units were classified as interneurons if they had an average firing rate exceeding 7 Hz and an average spike width under 0.3 ms. All other units were considered putative pyramidal cells. Units were excluded from analysis if they had fewer than 100 spikes across all sessions. A small number of pyramidal cells only had spikes during sleep epochs, and these were excluded from analysis[78,102] since all analysis done here focused exclusively on the task periods.

Task Responsiveness

Task responsiveness was calculated as a change in firing rate following odor onset, compared to a pre-stimulus period of the same length of time as the odor sampling period on each trial leading up to odor port engagement. Sampling events were only considered if the

animal held its nose in the odor port for longer than 0.50 seconds and proceeded to a reward port. Statistical significance was determined from the Wilcoxon signed rank test of those trial-matched rate differences for each odor identity separately. If a cell showed a significant change up or down from baseline for at least one of the odors, it was considered task responsive. Of note, there was only a single unit analyzed whose firing rate changed in opposite directions from baseline for the two odors, the remainder showed the same direction of change in firing rate for the two odors.

Choice Selectivity

Firing rates during odor sampling were calculated as the number of spikes as a function of time from odor-port engagement to odor-port disengagement. Choice selectivity was calculated using the following equation:

$$SI = \frac{\lambda_1 - \lambda_2}{\lambda_1 + \lambda_2}$$

Where λ_1 is the firing rate vector for Odor 1 trials, and λ_2 is firing rate vector for Odor 2 trials. *SI* = 1 indicates that the cell only responded on Odor 1 trials, whereas *SI* = -1 indicates that the cell only responded on Odor 2 trials. To determine significance, a null distribution was generated in which the odor identities were shuffled across trials. Cells were considered choice-selective if the SI fell outside of 1.5 s.d. from the mean of the null distribution.

Population Differential Index

806 The population differential index (PDI) was calculated as described in Igarashi et al.,
807 2014. For this analysis, all task-responsive cells were pooled across animals and days into a
808 single population. Mean firing rates were calculated in 100 ms bins from 0 to 1 second aligned
809 to odor onset to obtain population vectors for each of the two odors. At each time bin, the
810 correlation coefficient (CC) was calculated between the Odor 1 response vector and Odor 2
811 response vector. This CC was subtracted from 1 to obtain the PDI:

812 $$1 - CC = PDI$$

813 such that PDI = 1 indicates that the population responses for the two odors are completely
814 distinct, whereas PDI = 0 indicates that the responses are identical. Chance-level PDI was
815 computed by shuffling the odor identities across trials and creating a null distribution. The real
816 PDI was then compared to the null distribution across the odor sampling time window. The
817 timepoint at which the population responses considered significantly distinct from each other
818 was defined as the first timepoint at which the real PDI surpassed the 95% confidence interval
819 of the null distribution.

820

821 **Individual Trial PDI**

822 A similar PDI analysis was employed to examine population dynamics on a trial-by-trial
823 basis, in which the PDI was computed for single trials individually. Cells were not pooled across
824 animals, and only sessions with at least 3 task-responsive cells were considered for analysis.
825 The PDI was computed by calculating the CC between the trial PV and the average PV of all
826 trials of the opposite odor in that session.

827

828 **GLM**

A generalized liner model (GLM) with a log link function was constructed to predict reward choice based on neural activity during the odor sampling period. Activity from all task-responsive neurons that were active on at least 10 trials was included. Neural population activity from different length time bins from 0.1 seconds to 1 second aligned to odor onset was used for prediction, i.e. 0-0.1s, 0-0.2s … 0-1.0s. Five-fold cross validation was used to test prediction. For each fold, the session's trials were randomly partitioned into five equally sized sets. Four of the five sets were used to train the GLM model and the remaining set was used to test. The prediction accuracy was calculated by dividing the number of correctly predicted trials by the total number of trials used for testing for each fold.

Significance was determined by performing the same procedure as described above but shuffling the trial outcomes to obtain a null distribution. At each time bin used for the prediction, a rank-sum test was performed on the prediction accuracy using the real data compared to the shuffled data.

Phase Locking

For all phase-locking analyses, the tetrode in each region with the most cells on each given day was used to measure oscillatory phase of either beta or RR. Phase locking of individual cells to the beta and respiratory rhythms was calculated by pooling the spike phases of each cell during the odor-sampling periods and performing a Rayleigh Z test for circular non-uniformity. For each cell, the mean direction of the von Mises distribution of spike-phases was used as the preferred phase.

852 **Occupancy Maps**

853 For all spatial field analyses, only the 5 animals that were trained on the full T-maze
854 were used; the three animals trained on the truncated maze were excluded due to insufficient
855 spatial data. Two-dimensional occupancy maps were generated by calculating occupancy in 2-
856 cm square spatial bins from epochs in which the animals running speed exceeded 3 cm/sec and
857 convolving with a 2d Gaussian ($\boldsymbol{\sigma}$= 2 pixels).

858

859 **Place Field Determination**

860 2-D occupancy-normalized firing rate maps were generated by dividing the spikes at
861 each 2-D pixel by the unsmoothed occupancy at that pixel, and then and smoothing with a
862 Gaussian kernel of (σ = 2 pixels, or 4 cm).

863 Linearized trajectory occupancy maps were calculated as previously described[31,97,98]. Briefly,
864 the rats 2d spatial coordinates were first segmented into run epochs based on contiguous bouts
865 of time in which the animals running speed exceeded 3 cm/sec. Then, the position of the animal
866 during each 'run epoch' was categorized by its origin and destination, and each position was
867 assigned to one of 100 (1.23 cm) bins from the origin to the destination of that route. Then the
868 total number of spikes at each bin was divided by that bin's occupancy, and the map was
869 convolved by a Gaussian kernel with a standard deviation of 2 pixels (2.5 cm).

870 Place field peak was calculated as the peak rate bin on the smoothed, linearized rate map,
871 and place fields were only considered for trajectories in which the cell had a peak firing rate of at
872 least 1 Hz. Place field width was calculated using a flood fill-algorithm in which the edges were
873 defined as the closest bins to the peak bin in which the rate fell below 25% of the peak rate.
874 Place field sparsity and information scores were calculated as previously described[103]. A cell

875 was determined to have a place field if its peak firing rate along that trajectory was ≥ 2 S.D.
876 above the mean of a bootstrapped distribution generated by circularly shifting the spikes in time
877 for each individual run, and if the field covered less than 75% of the linearized trajectory. When
878 analyzing the place field characteristics of choice-selective cells (**Fig. 6**, **Supplementary Fig.**
879 **6**), the field of each outbound journey was analyzed separately so as to prevent 'choosing'
880 certain fields over others.

881

882 **Trajectory Selectivity**

883 Trajectory selective cells were identified using a previously validated method[31]. Briefly,
884 the linearized spatial tuning curve was calculated separately for each outbound trajectory and
885 the correlation between those trajectories was computed. A cell was identified as trajectory
886 selective if this correlation value exceeded the 95th percentile of a distribution wherein each
887 outbound trajectory identity was shuffled and the correlation recalculated.

888 To measure trajectory selectivity as it related to decision period selectivity, we used an
889 analogous method to the odor selectivity index. Briefly we calculated the mean firing rate along
890 each run beginning one half second following odor port exit and once the animals speed
891 exceeded 3 cm/sec to the end of that run (when the animal either reached the goal or its
892 velocity fell below 3 cm/sec for more than ½ second). The difference in these mean firing rates
893 across runs was divided by the sum of those two mean rates to generate a trajectory selectivity
894 index.

895

896 **Bayesian Decoder**

Choice identity decoding was performed as previously described[102]. Briefly, a memoryless Bayesian decoder was built for each of the two choice identities from spikes occurring in the odor sampling period. Then, the likelihood of each choice (x) was reconstructed from their posterior probabilities given the spikes occurring at each segment along the maze on each run (p(x | spikes) = p(spikes | x) * p(x) / p(spikes)). Run activity was defined as contiguous bouts following the odor sampling period when the animal was traveling above 3 cm/sec. Additionally, to prevent overlap between odor-period spiking and run spiking, the run periods were defined beginning 0.5 seconds following odor port disengagement time. We assumed that the N active cells fired independently and followed a Poisson process, giving the following equation.

$$P(X|spikes) = C * (\prod_{i=1}^{N} f_i(X)^{spikes_i}) * e^{-\tau} \sum_{i=1}^{N} f(X)$$

Where C is a normalization constant across the two choice identities. The p-value was calculated from the Gaussian statistics of a Monte Carlo random shuffle (200 shuffles) of choice identity during the odor sampling period. When choice identity decoding was calculated from the likelihoods of activity from each run, the decoding was performed in the same 5-fold leave-one-out fashion as was used in the GLM analyses, and the p value was calculated from the same Monte Carlo random shuffle of the training set route identities as the odor period based decoding.

Data Availability

The behavioral and electrophysiological data supporting the findings in this study are archived on servers at Brandeis University and are available upon request to the corresponding author.

Code Availability

All data processing, analyses and statistics in this study were conducted using open-source package Mountainsort (https://github.com/flatironinstitute/mountainsort) and custom code in MATLAB (R2018), unless otherwise noted. All custom code is available upon request to the corresponding author.

ACKNOWLEDGMENTS

This work was supported by NIH Grant R01MH120228, a Whitehall Foundation award, and a Smith Foundation Odyssey award to S.P.J. We thank the late Howard Eichenbaum for assistance with the behavioral task.

AUTHOR CONTRIBUTIONS

S.P.J. conceived and designed the study, C.A.S. performed experiments and analyzed the data, J.B. analyzed the data, E.K. contributed to experiments, S.P.J. and C.A.S. wrote the manuscript with input from all authors.

COMPETING INTERESTS STATEMENT

The authors declare no competing interests.

REFERENCES

1 Fitzgerald, J. K., Freedman, D. J. & Assad, J. A. Generalized associative representations in parietal cortex. *Nat Neurosci* **14**, 1075-1079, doi:10.1038/nn.2878 (2011).

2 Wirth, S. *et al.* Single neurons in the monkey hippocampus and learning of new associations. *Science* **300**, 1578-1581 (2003).

3 Wirth, S. *et al.* Trial outcome and associative learning signals in the monkey hippocampus. *Neuron.* **61**, 930-940 (2009).

4 Yanike, M., Wirth, S. & Suzuki, W. A. Representation of well-learned information in the monkey hippocampus. *Neuron.* **42**, 477-487 (2004).

5 Igarashi, K. M., Lu, L., Colgin, L. L., Moser, M. B. & Moser, E. I. Coordination of entorhinal-hippocampal ensemble activity during associative learning. *Nature* **510**, 143-147, doi:10.1038/nature13162 (2014).

6 Allen, T. A., Salz, D. M., Mckenzie, S. & Fortin, N. J. Nonspatial Sequence Coding in CA1 Neurons. *J Neurosci* **36**, 1547-1563 (2016).

7 McKenzie, S. *et al.* Hippocampal representation of related and opposing memories develop within distinct, hierarchically organized neural schemas. *Neuron* **83**, 202-215 (2014).

8 Otto, T. & Eichenbaum, H. Neuronal activity in the hippocampus during delayed non-match to sample performance in rats: evidence for hippocampal processing in recognition memory. *Hippocampus.* **2**, 323-334 (1992).

9 Moita, M. A., Rosis, S., Zhou, Y., LeDoux, J. E. & Blair, H. T. Hippocampal place cells acquire location-specific responses to the conditioned stimulus during auditory fear conditioning. *Neuron* **37**, 485-497 (2003).

10 Schoenbaum, G. & Eichenbaum, H. Information coding in the rodent prefrontal cortex. II. Ensemble activity in orbitofrontal cortex. *J Neurophysiol* **74**, 751-762 (1995).

11 Shadlen, M. N. & Newsome, W. T. Neural basis of a perceptual decision in the parietal cortex (area LIP) of the rhesus monkey. *J Neurophysiol* **86**, 1916-1936 (2001).

12 Harvey, C. D., Coen, P. & Tank, D. W. Choice-specific sequences in parietal cortex during a virtual-navigation decision task. *Nature* **484**, 62-68, doi:10.1038/nature10918 (2012).

13 Singer, A. C., Carr, M. F., Karlsson, M. P. & Frank, L. M. Hippocampal SWR activity predicts correct decisions during the initial learning of an alternation task. *Neuron* **77**, 1163-1173, doi:10.1016/j.neuron.2013.01.027 (2013).

14 Johnson, A. & Redish, A. D. Neural ensembles in CA3 transiently encode paths forward of the animal at a decision point. *Journal of Neuroscience* **27**, 12176-12189 (2007).

15 Floresco, S. B., Seamans, J. K. & Phillips, A. G. Selective roles for hippocampal, prefrontal cortical, and ventral striatal circuits in radial-arm maze tasks with or without a delay. *J Neurosci* **17**, 1880-1890 (1997).

16 Battaglia, F. P., Benchenane, K., Sirota, A., Pennartz, C. M. & Wiener, S. I. The hippocampus: hub of brain network communication for memory. *Trends Cogn Sci* **15**, 310-318, doi:10.1016/j.tics.2011.05.008 (2011).

17 Euston, D. R., Gruber, A. J. & McNaughton, B. L. The role of medial prefrontal cortex in memory and decision making. *Neuron* **76**, 1057-1070, doi:10.1016/j.neuron.2012.12.002 (2012).

18 Miller, E. K. & Cohen, J. D. An integrative theory of prefrontal cortex function. *Annu Rev Neurosci* **24**, 167-202, doi:10.1146/annurev.neuro.24.1.167 (2001).

19 Lee, I. & Solivan, F. The roles of the medial prefrontal cortex and hippocampus in a spatial paired-association task. *Learning & Memory* **15**, 357-367 (2008).

20 Wiener, S. I., Paul, C. A. & Eichenbaum, H. Spatial and behavioral correlates of hippocampal neuronal activity. *Journal of Neuroscience* **9**, 2737-2763 (1989).

21 Gothard, K. M., Skaggs, W. E., Moore, K. M. & McNaughton, B. L. Binding of hippocampal CA1 neural activity to multiple reference frames in a landmark-based navigation task. *J Neurosci* **16**, 823-835 (1996).

22 Hyman, J. M., Ma, L., Balaguer-Ballester, E., Durstewitz, D. & Seamans, J. K. Contextual encoding by ensembles of medial prefrontal cortex neurons. *Proc Natl Acad Sci U S A* **109**, 5086-5091 (2012).

23 Wiltgen, B. J., Brown, R. A., Talton, L. E. & Silva, A. J. New circuits for old memories: the role of the neocortex in consolidation. *Neuron* **44**, 101-108, doi:10.1016/j.neuron.2004.09.015 (2004).

24 Hasegawa, I. Neural mechanisms of memory retrieval: role of the prefrontal cortex. *Rev Neurosci* **11**, 113-125 (2000).

25 Siegle, J. H. & Wilson, M. A. Enhancement of encoding and retrieval functions through theta phase-specific manipulation of hippocampus. *Elife* **3**, e03061, doi:10.7554/eLife.03061 (2014).

26 Fortin, N. J., Wright, S. P. & Eichenbaum, H. Recollection-like memory retrieval in rats is dependent on the hippocampus. *Nature* **431**, 188-191 (2004).

27 Cenquizca, L. A. & Swanson, L. W. Spatial organization of direct hippocampal field CA1 axonal projections to the rest of the cerebral cortex. *Brain Res Rev.* **56**, 1-26 (2007).

28 Ito, H. T., Zhang, S. J., Witter, M. P., Moser, E. I. & Moser, M. B. A prefrontal-thalamo-hippocampal circuit for goal-directed spatial navigation. *Nature* **522**, 50-55, doi:10.1038/nature14396 (2015).

29 Delatour, B. & Witter, M. P. Projections from the parahippocampal region to the prefrontal cortex in the rat: evidence of multiple pathways. *Eur J Neurosci* **15**, 1400--1407 (2002).

30 Shin, J. D. & Jadhav, S. P. Multiple modes of hippocampal-prefrontal interactions in memory-guided behavior. *Curr. Opin. Neurobiol.* **40**, 161-169, doi:10.1016/j.conb.2016.07.015 (2016).

31 Shin, J. D., Tang, W. & Jadhav, S. P. Dynamics of Awake Hippocampal-Prefrontal Replay for Spatial Learning and Memory-Guided Decision Making. *Neuron* **104**, 1110-1125 (2019).

32 Yu, J. Y. & Frank, L. M. Hippocampal-cortical interaction in decision making. *Neurobiol Learn Mem* **117**, 34-41, doi:10.1016/j.nlm.2014.02.002 (2015).

33 Zielinski, M. C., Tang, W. & Jadhav, S. P. The role of replay and theta sequences in mediating hippocampal-prefrontal interactions for memory and cognition. *Hippocampus*, doi:10.1002/hipo.22821 (2017).

34 Place, R., Farovik, A., Brockmann, M. & Eichenbaum, H. Bidirectional prefrontal-hippocampal interactions support context-guided memory. *Nat Neurosci*, doi:10.1038/nn.4327 (2016).

35 Maharjan, D. M., Dai, Y. Y., Glantz, E. H. & Jadhav, S. P. Disruption of dorsal hippocampal - prefrontal interactions using chemogenetic inactivation impairs spatial learning. *Neurobiol Learn Mem* **155**, 351-360, doi:10.1016/j.nlm.2018.08.023 (2018).

36 Colgin, L. L. Oscillations and hippocampal-prefrontal synchrony. *Curr Opin Neurobiol* **21**, 467-474, doi:10.1016/j.conb.2011.04.006 (2011).

37 Gordon, J. A. Oscillations and hippocampal-prefrontal synchrony. *Curr Opin Neurobiol* **21**, 486-491, doi:10.1016/j.conb.2011.02.012 (2011).

38 Jones, M. W. & Wilson, M. A. Theta rhythms coordinate hippocampal-prefrontal interactions in a spatial memory task. *PLoS.Biol.* **3**, e402 (2005).

39 Buzsaki, G. & Draguhn, A. Neuronal oscillations in cortical networks. *Science.* **304**, 1926-1929 (2004).

40 Benchenane, K., Tiesinga, P. H. & Battaglia, F. P. Oscillations in the prefrontal cortex: a gateway to memory and attention. *Curr Opin Neurobiol* **21**, 475-485, doi:10.1016/j.conb.2011.01.004 (2011).

41 Hyman, J. M., Zilli, E. A., Paley, A. M. & Hasselmo, M. E. Working Memory Performance Correlates with Prefrontal-Hippocampal Theta Interactions but not with Prefrontal Neuron Firing Rates. *Front Integr Neurosci* **4**, 2, doi:10.3389/neuro.07.002.2010 (2010).

42 Benchenane, K. *et al.* Coherent theta oscillations and reorganization of spike timing in the hippocampal-prefrontal network upon learning. *Neuron* **66**, 921-936, doi:10.1016/j.neuron.2010.05.013 (2010).

43 Abraham, N. M. *et al.* Maintaining accuracy at the expense of speed: Stimulus similarity defines odor discrimination time in mice. *Neuron* **44**, 865-876 (2004).

44 Rinberg, D., Koulakov, A. & Gelperin, A. Speed-accuracy tradeoff in olfaction. *Neuron* **51**, 351-358, doi:10.1016/j.neuron.2006.07.013 (2006).

1042 45 Uchida, N. & Mainen, Z. F. Speed and accuracy of olfactory discrimination in the rat. *Nat*
1043 *Neurosci* **6**, 1224-1229, doi:10.1038/nn1142 (2003).

1044 46 Eichenbaum, H. Using olfaction to study memory. *Ann N Y Acad Sci* **855**, 657-669 (1998).

1045 47 Frederick, D. E. *et al.* Gamma and Beta Oscillations Define a Sequence of Neurocognitive Modes
1046 Present in Odor Processing. *J Neurosci* **36**, 7750-7767 (2016).

1047 48 Kay, L. M. & Beshel, J. A beta oscillation network in the rat olfactory system during a 2-
1048 alternative choice odor discrimination task. *J Neurophysiol* **104**, 829-839,
1049 doi:10.1152/jn.00166.2010 (2010).

1050 49 Rangel, L. M. *et al.* Rhythmic coordination of hippocampal neurons during associative memory
1051 processing. *Elife* **5**, doi:10.7554/eLife.09849 (2016).

1052 50 Stopfer, M., Jayaraman, V. & Laurent, G. Intensity versus identity coding in an olfactory system.
1053 *Neuron* **39**, 991-1004 (2003).

1054 51 Nguyen Chi, V. *et al.* Hippocampal Respiration-Driven Rhythm Distinct from Theta Oscillations in
1055 Awake Mice. *J Neurosci* **36**, 162-177 (2016).

1056 52 Kepecs, A., Uchida, N. & Mainen, Z. F. The Sniff as a Unit of Olfactory Processing. *Chemical*
1057 *Senses* **31**, 167-179 (2006).

1058 53 Lockmann, A. L. V., Laplagne, D. A., Leão, R. N. & Tort, A. B. L. A Respiration-Coupled Rhythm in
1059 the Rat Hippocampus Independent of Theta and Slow Oscillations. *J Neurosci* **36**, 5338-5352
1060 (2016).

1061 54 Verhagen, J. V., Wesson, D. W., Netoff, T. I., White, J. a. & Wachowiak, M. Sniffing controls an
1062 adaptive filter of sensory input to the olfactory bulb. *Nature Neuroscience* **10**, 631-639 (2007).

1063 55 Kay, L. M. Theta oscillations and sensorimotor performance. *Proc. Natl. Acad. Sci. U.S.A* **102**,
1064 3863-3868 (2005).

1065 56 Fujisawa, S., Amarasingham, A., Harrison, M. T. & Buzsaki, G. Behavior-dependent short-term
1066 assembly dynamics in the medial prefrontal cortex. *Nat Neurosci* **11**, 823-833,
1067 doi:10.1038/nn.2134 (2008).

1068 57 Fujisawa, S. & Buzsaki, G. A 4 Hz oscillation adaptively synchronizes prefrontal, VTA, and
1069 hippocampal activities. *Neuron* **72**, 153-165, doi:S0896-6273(11)00739-2 [pii]
1070 10.1016/j.neuron.2011.08.018 (2011).

1071 58 Martin, C., Beshel, J. & Kay, L. M. An olfacto-hippocampal network is dynamically involved in
1072 odor-discrimination learning. *J Neurophysiol* **98**, 2196-2205, doi:10.1152/jn.00524.2007 (2007).

1073 59 Alvarez, P., Wendelken, L. & Eichenbaum, H. Hippocampal formation lesions impair performance
1074 in an odor-odor association task independently of spatial context. *Neurobiol. Learn. Mem.* **78**,
1075 470-476 (2002).

1076 60 Peters, G. J., David, C. N., Marcus, M. D. & Smith, D. M. The medial prefrontal cortex is critical
1077 for memory retrieval and resolving interference. *Learning & Memory* **20**, 201-209 (2013).

1078 61 Otto, T. & Eichenbaum, H. Complementary roles of the orbital prefrontal cortex and the
1079 perirhinal- entorhinal cortices in an odor-guided delayed-nonmatching-to-sample task. *Behav*
1080 *Neurosci* **106**, 762-775 (1992).

1081 62 Eichenbaum, H., Fagan, A. & Cohen, N. J. Normal olfactory discrimination learning set and
1082 facilitation of reversal learning after medial-temporal damage in rats: implications for an
1083 account of preserved learning abilities in amnesia. *J Neurosci* **6**, 1876-1884 (1986).

1084 63 Moser, M. B. & Moser, E. I. Distributed encoding and retrieval of spatial memory in the
1085 hippocampus. *J Neurosci* **18**, 7535--7542 (1998).

1086 64 Wiltgen, B. J. *et al.* The hippocampus plays a selective role in the retrieval of detailed context
1087 memories. *Curr Biol* **20**, 1336-1344 (2010).

1088 65 Churchwell, J. C., Morris, A. M., Musso, N. D. & Kesner, R. P. Prefrontal and hippocampal
1089 contributions to encoding and retrieval of spatial memory. *Neurobiol Learn Mem* **93**, 415-421,
1090 doi:10.1016/j.nlm.2009.12.008 (2010).

1091 66 Kay, L. M. in *Progress in Brain Research* Vol. 208 (ed Donald A. Wilson Edi Barkai) (Elsevier,
1092 2014).

1093 67 Kay, L. M. *et al.* Olfactory oscillations: the what, how and what for. *Trends in Neurosciences* **32**,
1094 207-214 (2009).

1095 68 Neville, K. R. & Haberly, L. B. Beta and Gamma Oscillations in the Olfactory System of the
1096 Urethane-Anesthetized Rat. *Journal of Neurophysiology* **90**, 3921-3930 (2003).

1097 69 Martin, C., Gervais, R., Messaoudi, B. & Ravel, N. Learning-induced oscillatory activities
1098 correlated to odour recognition: a network activity. *European Journal of Neuroscience* **23**, 1801-
1099 1810 (2006).

1100 70 Donoghue, J. P., Sanes, J. N., Hatsopoulos, N. G. & Gaál, G. Neural discharge and local field
1101 potential oscillations in primate motor cortex during voluntary movements. *Journal of*
1102 *Neurophysiology* **79**, 159-173 (1998).

1103 71 Sanes, J. N. & Donoghue, J. P. Oscillations in local field potentials of the primate motor cortex
1104 during voluntary movement. *Proc Natl Acad Sci U S A* **90**, 4470-4474 (1993).

1105 72 Carr, M. F., Jadhav, S. P. & Frank, L. M. Hippocampal replay in the awake state: a potential
1106 substrate for memory consolidation and retrieval. *Nat Neurosci* **14**, 147-153,
1107 doi:10.1038/nn.2732 (2011).

1108 73 Joo, H. R. & Frank, L. M. The hippocampal sharp wave-ripple in memory retrieval for immediate
1109 use and consolidation. *Nat Rev Neurosci* **19**, 744-757, doi:10.1038/s41583-018-0077-1 (2018).

74 Norman, Y. *et al.* Hippocampal sharp-wave ripples linked to visual episodic recollection in humans. *Science* **365**, doi:10.1126/science.aax1030 (2019).

75 Buzsaki, G., Leung, L. W. & Vanderwolf, C. H. Cellular bases of hippocampal EEG in the behaving rat. *Brain Res.* **287**, 139-171 (1983).

76 Schoenbaum, G. & Eichenbaum, H. Information coding in the rodent prefrontal cortex. I. Single-neuron activity in orbitofrontal cortex compared with that in pyriform cortex. *J.Neurophysiol.* **74**, 733-750 (1995).

77 Taxidis, J. *et al.* Differential Emergence and Stability of Sensory and Temporal Representations in Context-Specific Hippocampal Sequences. *Neuron* **108**, 1-15 (2020).

78 Jadhav, S. P., Rothschild, G., Roumis, D. K. & Frank, L. M. Coordinated excitation and inhibition of prefrontal ensembles during awake hippocampal sharp-wave ripple events. *Neuron* **90**, 113-127, doi:10.1016/j.neuron.2016.02.010 (2016).

79 Siapas, A. G., Lubenov, E. V. & Wilson, M. A. Prefrontal phase locking to hippocampal theta oscillations. *Neuron* **46**, 141-151, doi:10.1016/j.neuron.2005.02.028 (2005).

80 Tort, A. B., Komorowski, R. W., Manns, J. R., Kopell, N. J. & Eichenbaum, H. Theta-gamma coupling increases during the learning of item-context associations. *Proc Natl Acad Sci U S A* **106**, 20942-20947, doi:0911331106 [pii]10.1073/pnas.0911331106 (2009).

81 Hermer-Vazquez, R., Hermer-Vazquez, L., Srinivasan, S. & Chapin, J. K. Beta- and gamma-frequency coupling between olfactory and motor brain regions prior to skilled, olfactory-driven reaching. *Experimental Brain Research* **180**, 217-235 (2007).

82 Buzsáki, G. Hippocampal sharp wave-ripple: A cognitive biomarker for episodic memory and planning. *Hippocampus* **25**, 1073-1188, doi:10.1002/hipo.22488 (2015).

83 Beshel, J., Kopell, N. & Kay, L. M. Olfactory bulb gamma oscillations are enhanced with task demands. *J Neurosci* **27**, 8358-8365, doi:10.1523/JNEUROSCI.1199-07.2007 (2007).

84 Martin, C. & Ravel, N. Beta and gamma oscillatory activities associated with olfactory memory tasks: different rhythms for different functional networks? *Frontiers in Behavioral Neuroscience* **8** (2014).

85 Eichenbaum, H., Kuperstein, M., Fagan, A. & Nagode, J. Cue-sampling and goal-approach correlates of hippocampal unit activity in rats performing an odor-discrimination task. *J Neurosci* **7**, 716-732 (1987).

86 Terada, S., Sakurai, Y., Nakahara, H. & Fujisawa, S. Temporal and Rate Coding for Discrete Event Sequences in the Hippocampus. *Neuron* **94**, 1248-1262 (2017).

87 Komorowski, R. W., Manns, J. R. & Eichenbaum, H. Robust conjunctive item-place coding by hippocampal neurons parallels learning what happens where. *J Neurosci* **29**, 9918-9929 (2009).

88 Ferbinteanu, J., Shirvalkar, P. & Shapiro, M. L. Memory modulates journey-dependent coding in the rat hippocampus. *J Neurosci* **31**, 9135-9146, doi:10.1523/JNEUROSCI.1241-11.2011 (2011).

89 Liu, X. *et al.* Optogenetic stimulation of a hippocampal engram activates fear memory recall. *Nature* **484**, 381-385, doi:10.1038/nature11028 (2012).

90 DeNardo, L. A. *et al.* Temporal evolution of cortical ensembles promoting remote memory retrieval. *Nat Neurosci* **22**, 460-469 (2019).

91 Buschman, T. J., Denovellis, E. L., Diogo, C., Bullock, D. & Miller, E. K. Synchronous oscillatory neural ensembles for rules in the prefrontal cortex. *Neuron* **76**, 838-846, doi:10.1016/j.neuron.2012.09.029 (2012).

92 Papale, A. E., Zielinski, M. C., Frank, L. M., Jadhav, S. P. & Redish, A. D. Interplay between hippocampal sharp-wave-ripple events and vicarious trial and error behaviors in decision making. *Neuron* **92**, 975-982, doi:10.1016/j.neuron.2016.10.028 (2016).

93 Wikenheiser, A. M. & Redish, A. D. Hippocampal theta sequences reflect current goals. *Nat. Neurosci.* **18**, 289-294 (2015).

94 Zielinski, M. C., Shin, J. D. & Jadhav, S. P. Coherent Coding of Spatial Position Mediated by Theta Oscillations in the Hippocampus and Prefrontal Cortex. *J Neurosci* **39**, 4550-4565, doi:10.1523/JNEUROSCI.0106-19.2019 (2019).

95 Zhong, W. *et al.* Selective entrainment of gamma subbands by different slow network oscillations. *Proc Natl Acad Sci U S A* **114**, 4519-4524 (2017).

96 Lisman, J. E. & Jensen, O. The theta-gamma neural code. *Neuron* **77**, 1002-1016 (2013).

97 Jadhav, S. P., Kemere, C., German, P. W. & Frank, L. M. Awake hippocampal sharp-wave ripples support spatial memory. *Science* **336**, 1454-1458, doi:10.1126/science.1217230 (2012).

98 Tang, W., Shin, J. D., Frank, L. M. & Jadhav, S. P. Hippocampal-prefrontal reactivation during learning is stronger in awake compared with sleep states. *J Neurosci* **37**, 11789-11805, doi:10.1523/JNEUROSCI.2291-17.2017 (2017).

99 Tort, A. B., Komorowski, R., Eichenbaum, H. & Kopell, N. Measuring phase-amplitude coupling between neuronal oscillations of different frequencies. *J Neurophysiol* **104**, 1195-1210, doi:jn.00106.2010 [pii] 10.1152/jn.00106.2010 (2010).

100 Barnett, A. H., Magland, J. F. & Greengard, L. F. Validation of Neural Spike Sorting Algorithms Without Ground-Truth Information. *J Neurosci Methods* **264**, 65-77 (2016).

101 Chung, J. E. *et al.* A Fully Automated Approach to Spike Sorting. *Neuron* **95**, 1381-1394 (2017).

102 Karlsson, M. P. & Frank, L. M. Awake replay of remote experiences in the hippocampus. *Nat. Neurosci.* **12**, 913-918, doi:10.1038/nn.2344 (2009).

103 Skaggs, W. E., McNaughton, B. L., Gothard, K. & Markus, E. in *Advanced in Neural Information Processing Systems* (eds S. Hanson, J. D. Cowan, & C. L. Giles) 1030-1037 (Morgan Kaufmann Publishers, 1993).

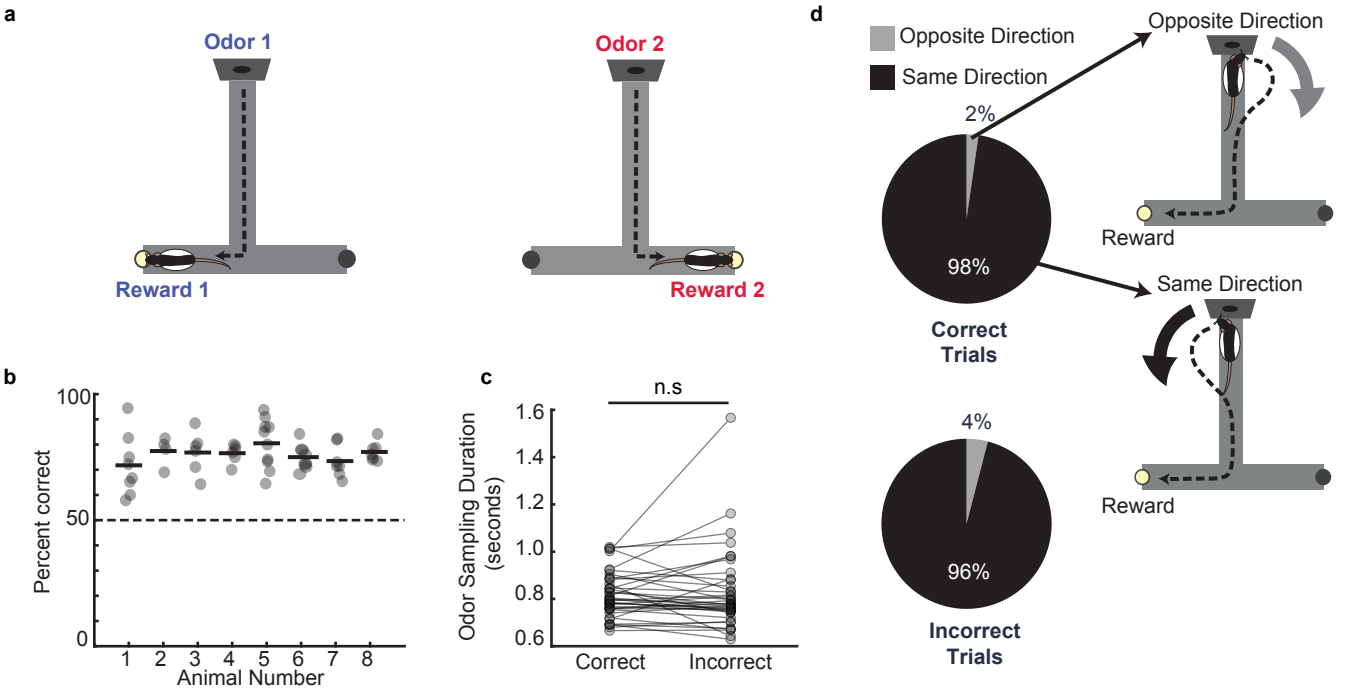
a
Odor 1
Reward 1
Odor 2
Reward 2
b
Percent correct
100
50
0
1 2 3 4 5 6 7 8
Animal Number
c
n.s
Odor Sampling Duration (seconds)
1.6
1.4
1.2
1.0
0.8
0.6
Correct
Incorrect
d
Opposite Direction
Same Direction
2%
98%
Correct Trials
4%
96%
Incorrect Trials
Opposite Direction
Reward
Same Direction
Reward

1180 **Figure 1: Odor–place associative memory and decision-making task**

1181 a. Schematic of the odor-cued T-maze task. Odors 1 (heptanol) and 2 (ethyl butyrate) were
1182 delivered at the odor port in pseudo-random order. Presentation of Odors 1 and 2 was
1183 associated with milk reward at Reward locations 1 and 2, respectively. Animals had to recall
1184 odor-space associations on each trial and utilize the association to choose the correct
1185 reward location.

1186 b. Performance of each animal (*n* = 8) on the odor-cued T-maze task (animals 1 - 5) or
1187 truncated odor-cued task (animals 6 - 8; truncated task, without spatial delay period) across
1188 multiple sessions (grey dots). Animal average is indicated by black bars. Dashed line
1189 indicates chance level.

1190 c. Odor sampling duration across all sessions (n = 38) on correct and incorrect trials (signed-
1191 rank test, p = 0.71).

1192 d. Turn direction away from odor port in relation to chosen reward well. Pie charts indicate the
1193 fraction of trials in which, at the odor port, animals turned in the same direction versus the
1194 opposite direction as the reward well that they would ultimately choose. Sessions in which
1195 animals ran the truncated task without spatial delay period were excluded. (correct trials: n =
1196 1624 same direction, 32 opposite direction, binomial test, p = 0; incorrect trials: n = 499
1197 same direction, 21 opposite direction, p = 1.4e-108).

1198

1199

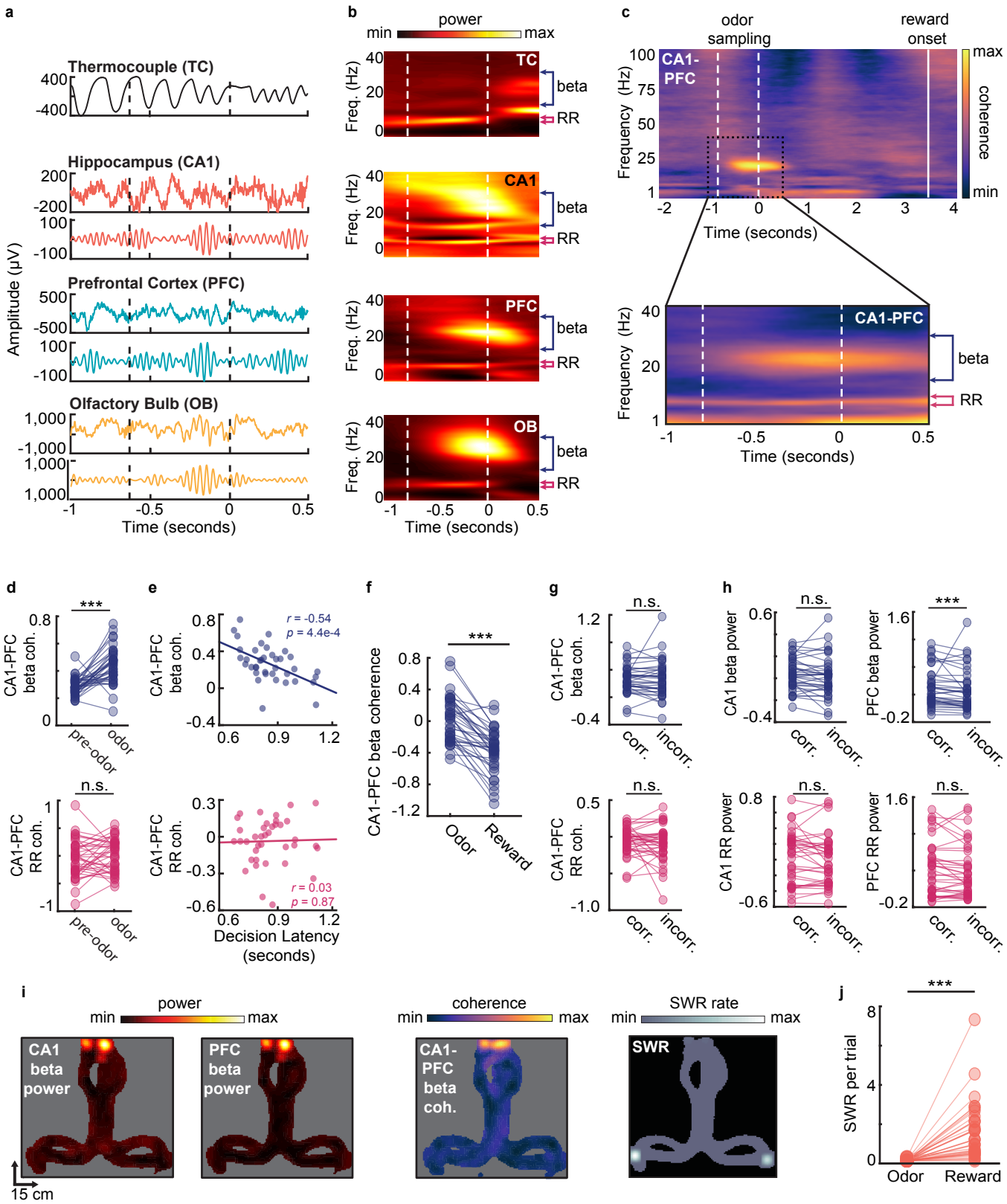
a
Thermocouple (TC)
Hippocampus (CA1)
Prefrontal Cortex (PFC)
Olfactory Bulb (OB)
Amplitude (μV)
Time (seconds)
b
power
min
max
TC
CA1
PFC
OB
beta
RR
Freq. (Hz)
Time (seconds)
c
odor sampling
reward onset
CA1-PFC
Frequency (Hz)
coherence
Time (seconds)
d
CA1-PFC beta coh.
CA1-PFC RR coh.
pre-odor
odor
n.s.
e
r = -0.54
p = 4.4e-4
r = 0.03
p = 0.87
Decision Latency (seconds)
f
CA1-PFC beta coherence
Odor
Reward
g
corr.
incorr.
h
CA1 beta power
PFC beta power
CA1 RR power
PFC RR power
i
CA1 beta power
PFC beta power
CA1-PFC beta coh.
SWR
SWR rate
15 cm
j
SWR per trial

Figure 2: Beta rhythms support decision making based on odor-place associations

a. Examples of thermocouple and LFP traces from one tetrode in each region during presentation of odor from one trial, aligned to odor port disengagement. Area between dashed lines indicates odor sampling period. Top to bottom: Respiratory rhythm recorded via thermocouple, CA1 signal, beta band (15-30 Hz) filtered CA1 signal, PFC signal, beta band filtered PFC signal, OB signal, beta band filtered OB signal.
b. Time-frequency plot showing power spectra aligned to odor offset. Color scale represents z-scored power. Area between dashed lines indicates average odor sampling period. Beta band is marked by blue bracket (15-30 Hz). RR band is marked by pink bracket (7-8 Hz). Thermocouple signal (TC), n = 12 sessions, max 0.69, min -0.31; CA1: n = 38 sessions, max 0.26, min -0.35; PFC: n = 38 sessions, max 0.60, min -0.16; and OB: n = 38 sessions, max 2.17, min -0.24.
c. Top: CA1-PFC coherence spectra for one animal during the full task time window from odor sampling (area between white dashed lines, aligned to odor offset) to average reward onset time (solid line) (n = 4 sessions, max 0.84; min -0.41). Bottom: CA1-PFC coherence aligned to odor offset across all animals (n = 38 sessions, max 0.51; min -0.34). Color scale represents z-scored power.
d. Beta (top) and RR (bottom) CA1-PFC coherence during odor periods and time-matched pre-odor periods. (signed-rank tests, n = 38 sessions. Beta coherence: p = 6.7e-6***; RR coherence: p = 0.36).
e. Beta (top) and RR (bottom) CA1-PFC coherence as a function of decision latency on correct trials. (n = 38 sessions, beta coherence: r = -0.54, p = 4.4e-4***; RR coherence: r = 0.03, p = 0.87).
f. CA1-PFC beta coherence during 500 ms window preceding odor port exit, and 500 ms window preceding reward well exit (signed rank test, n = 38 sessions, p = 1.2e-7***).

g. Beta (top) and RR (bottom) CA1-PFC coherence on correct and incorrect trials. (Signed-rank tests, n = 38 sessions. Beta coherence: p = 0.38; RR coherence: p = 0.81).

h. Beta (top row) and respiratory rhythm (RR) (bottom row) power on correct and incorrect trials in CA1 and PFC. (Signed-rank tests. n = 38 sessions. Beta power: CA1: p = 0.08; PFC: p = 8.3e-4***. RR power: CA1: p = 0.26; PFC: p = 0.16.)

i. Maps of T-maze showing the spatial distribution of z-scored CA1 beta power (left. max 1.49; min -0.19), PFC beta power (middle-left, max 1.63; min -0.18), CA1-PFC beta coherence (middle-right, max 1.16; min -0.19), and SWR rate (right, max 1.34; min 0). Plots are for a single session from one animal.

j. Number of SWR events per trial during odor sampling and reward consumption on correct trials (signed-rank test, n = 38 sessions, p =1.1e-7***).

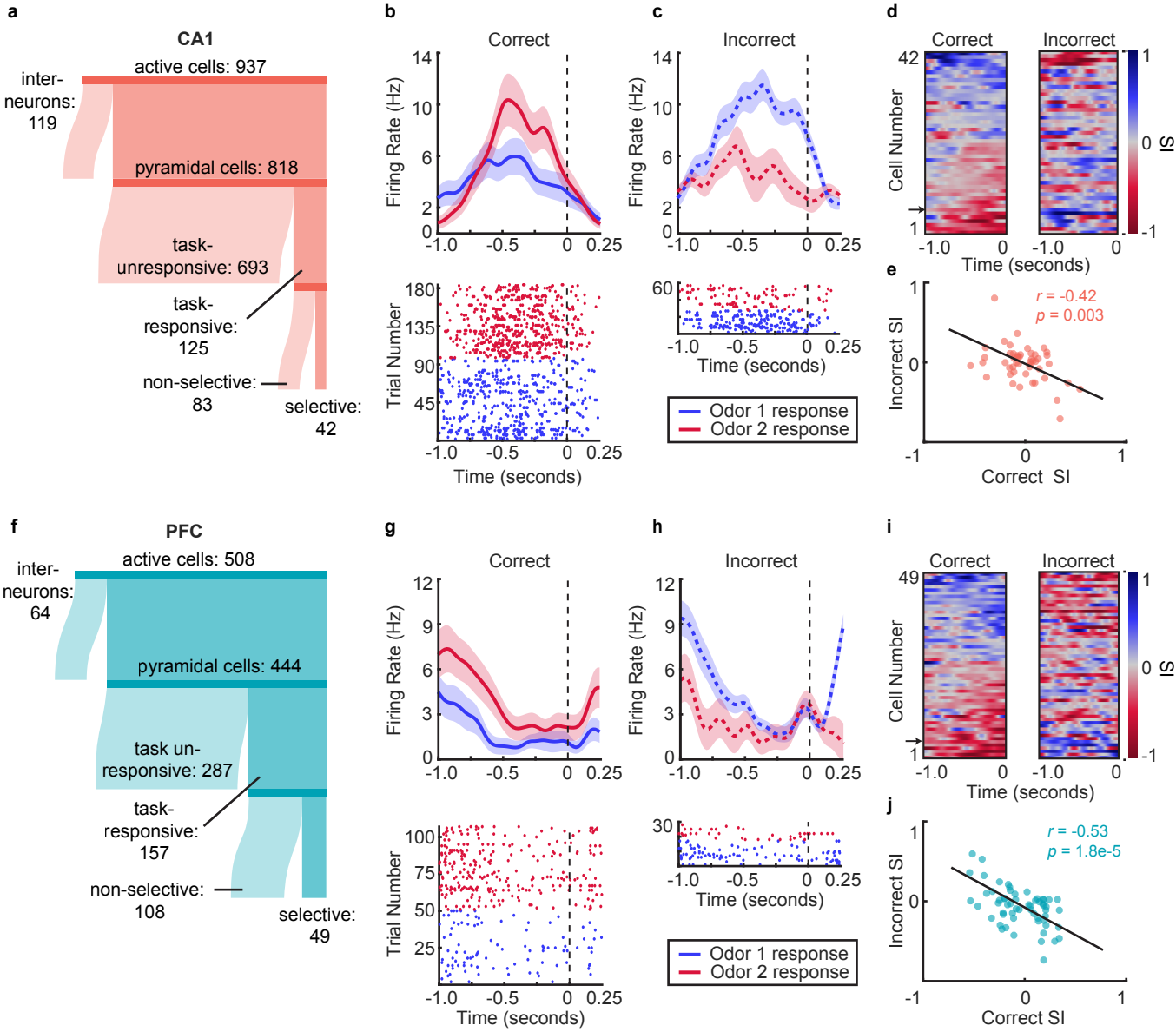
a
CA1
active cells: 937
inter-neurons: 119
pyramidal cells: 818
task-unresponsive: 693
task-responsive: 125
non-selective: 83
selective: 42
b
Correct
Firing Rate (Hz)
Trial Number
Time (seconds)
c
Incorrect
Firing Rate (Hz)
Time (seconds)
Odor 1 response
Odor 2 response
d
Correct
Incorrect
Cell Number
Time (seconds)
SI
e
r = -0.42
p = 0.003
Incorrect SI
Correct SI
f
PFC
active cells: 508
inter-neurons: 64
pyramidal cells: 444
task un-responsive: 287
task-responsive: 157
non-selective: 108
selective: 49
g
Correct
Firing Rate (Hz)
Trial Number
Time (seconds)
h
Incorrect
Firing Rate (Hz)
Time (seconds)
Odor 1 response
Odor 2 response
i
Correct
Incorrect
Cell Number
Time (seconds)
SI
j
r = -0.53
p = 1.8e-5
Incorrect SI
Correct SI

Figure 3: Single neurons in CA1 and PFC exhibit choice-selectivity during decision-making period

a. Sankey diagram showing the number of CA1 cells that were classified into different categories. Sizes of partitions are proportional to raw numbers.
b. Example PSTH and raster plot for a single choice-selective CA1 neuron on correct trials, aligned to odor-port disengagement. Shaded areas indicate s.e.m. Firing rates are shown in Hz, referring to spikes/second.
c. PSTH and raster plot for the same neuron in (b), but only for incorrect trials.
d. Selectivity index (SI) of all choice-selective cells in CA1 on correct trials (left) and incorrect trials (right), aligned to odor-port disengagement. SI is calculated as the difference in firing rate between Odor 1 trials and Odor 2 trials, divided by the sum of these firing rates. SI is color coded, where blue indicates an SI of 1 (absolute Choice 1 preference), red indicates an SI of -1 (absolute Choice 2 preference) and grey indicates an SI of 0 (not selective). Cells are sorted according to peak selectivity on correct trials and sorting order is the same for both plots.
e. Correlation between correct trial SI and incorrect trial SI for all choice-selective CA1 cells ($n = 42$, $r = -0.42$, $p = 0.003$**).

f-j. Same as a-e, but for PFC cells. Correlation in j: $n = 49$, $r = -0.53$, $p = 1.8e-5$***.

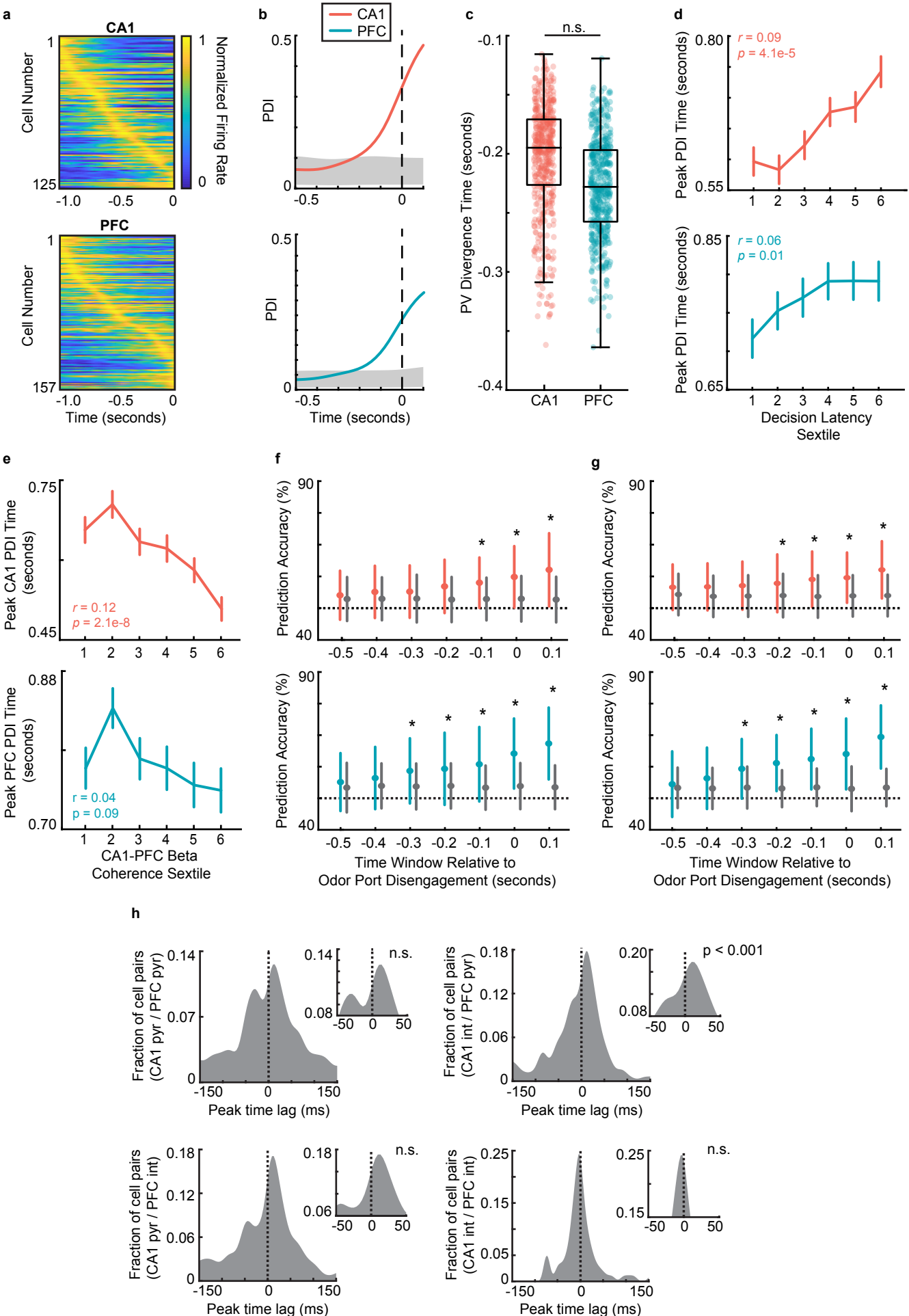
a
CA1
Cell Number
Normalized Firing Rate
PFC
Time (seconds)
b
CA1
PFC
PDI
Time (seconds)
c
n.s.
PV Divergence Time (seconds)
CA1
PFC
d
r = 0.09
p = 4.1e-5
Peak PDI Time (seconds)
r = 0.06
p = 0.01
Decision Latency Sextile
e
Peak CA1 PDI Time (seconds)
r = 0.12
p = 2.1e-8
Peak PFC PDI Time (seconds)
r = 0.04
p = 0.09
CA1-PFC Beta Coherence Sextile
f
Prediction Accuracy (%)
Time Window Relative to Odor Port Disengagement (seconds)
g
Prediction Accuracy (%)
Time Window Relative to Odor Port Disengagement (seconds)
h
Fraction of cell pairs (CA1 pyr / PFC pyr)
Peak time lag (ms)
n.s.
Fraction of cell pairs (CA1 int / PFC pyr)
p < 0.001
Fraction of cell pairs (CA1 pyr / PFC int)
n.s.
Fraction of cell pairs (CA1 int / PFC int)
n.s.

1258 **Figure 4: Neural ensemble responses during decision making are governed by beta**
1259 **coordination and predict the upcoming choice**

1260 a. Normalized firing rate of all task-responsive cells in CA1 (top) and PFC (bottom) during a 1
1261 second window before odor port disengagement.
1262 b. Discriminability between population vectors (PVs) on Odor 1 versus Odor 2 presentations,
1263 for CA1 task-responsive population (top, n = 125 cells) and PFC task-responsive
1264 population (bottom, n = 157 cells), across time bins aligned to odor port disengagement.
1265 Dissimilarity between PVs is scaled and shown as a PV differential index (PDI), where 0
1266 indicates identical responses. Colored line indicates real data, grey shaded area indicates
1267 95% confidence intervals of shuffled distribution.
1268 c. PV divergence time in CA1 and PFC. Divergence time is quantified as the first time point
1269 where the real data PDI surpasses the mean + 2 s.d. of the shuffled PDI distribution.
1270 Bootstrap test, n = 50 samples with replacement, 500 iterations. Boxplots indicate
1271 interquartile ranges of bootstrapped distributions. CA1: median = 0.19 seconds prior to
1272 odor-port disengagement, interquartile range = 0.06; PFC: median = 0.23 seconds prior to
1273 odor-port disengagement, interquartile range = 0.06; (bootstrap test; p = 0.31)
1274 d. Timing of peak PV discriminability (PDI) on each trial aligned to odor onset as a function of
1275 decision latency for CA1 (top) and PFC (bottom). Decision latencies were divided into six
1276 equally sized subgroups (sextiles) for visualization, but correlation coefficients were
1277 calculated using trials. Error bars show s.e.m. at each sextile (CA1: n = 2071 trials, r =
1278 0.16, p = 1.1e-12***; PFC: n = 2081 trials, r = r = 0.06, p = 0.007**). Individual trial rasters
1279 in Supplementary Figure 4j.
1280 e. Timing of peak PV discriminability (PDI) on each trial as a function of beta coherence. Beta
1281 coherence distribution was divided into six equally sized subgroups (sextiles) for

1282 visualization, but correlation coefficients were calculated using trials. Error bars show
1283 s.e.m. at each sextile (CA1: r = -0.12, p = 2.1e-8***; PFC: r = -0.04, p = 0.09).
1284 f. Prediction of animal's choice of reward well by a GLM according to ensemble activity
1285 during odor sampling across varying length time windows aligned to decision time. Colored
1286 error bars indicate real data mean ± s.d., whereas grey error bars indicate shuffled data
1287 mean ± s.d. Cells used for prediction include all task-responsive putative pyramidal cells in
1288 CA1 (left) and PFC (right). Stars indicate prediction time windows where the fraction of
1289 correctly predicted trials was significantly higher than the fraction from the shuffled data
1290 (rank-sum tests, * = $p < 0.05$).
1291 g. As in (i) but including both putative pyramidal and interneurons in ensembles for GLM
1292 prediction.
1293 h. Histograms showing distributions of peak timings of cross-correlations between CA1 and
1294 PFC cell pairs. Peaks falling above zero indicate CA1 leading, whereas peaks falling below
1295 zero indicate PFC leading. One-sample Wilcoxson signed rank tests (H_0: $\mu = 0$ ms). Top-
1296 left: CA1-PFC pyramidal pairs, n = 603 pairs, p = 0.07; top-right: CA1 interneuron-PFC
1297 pyramidal pairs, n = 462 pairs, p = 6.0e-4***; bottom-left: CA1 pyramidal-PFC interneuron
1298 pairs, n = 130 pairs, p = 0.14, bottom right: CA1-PFC interneuron pairs, n = 85 pairs, p =
1299 0.33.

1300

1301

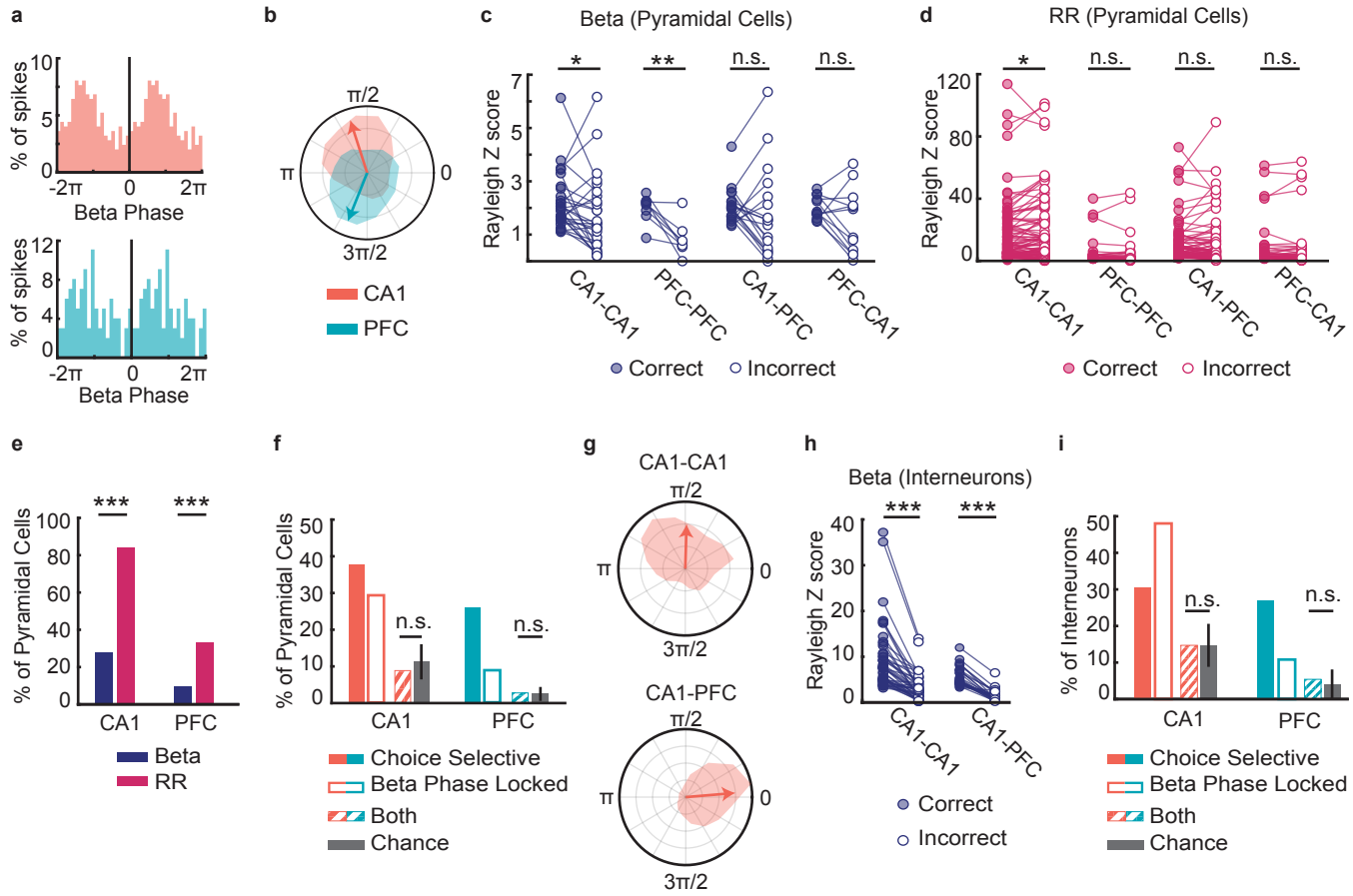
a
% of spikes
Beta Phase
b
π/2
π
0
3π/2
CA1
PFC
c
Beta (Pyramidal Cells)
Rayleigh Z score
CA1-CA1
PFC-PFC
CA1-PFC
PFC-CA1
Correct
Incorrect
d
RR (Pyramidal Cells)
e
% of Pyramidal Cells
Beta
RR
f
Choice Selective
Beta Phase Locked
Both
Chance
g
CA1-CA1
CA1-PFC
h
Beta (Interneurons)
i
% of Interneurons

Figure 5: CA1 and PFC cells phase lock to beta and respiratory rhythms during decision making

a. Example spike-phase histograms from two example cells that are phase locked to the beta rhythm. Top: CA1 cell (Rayleigh Z test, n = 242 spikes, z = 15.5, p = 1.5e-7); bottom: PFC cell (n = 99 spikes, z = 4.86, p = 0.007). Phase axes are duplicated for visibility.

b. Polar histogram of preferred beta phases for all task-responsive CA1 (n = 125 cells, Rayleigh Z test, z = 7.9, p = 3.4e-4) and PFC (n = 157 cells, z = 5.0, p = 0.006) cells. Arrows indicate mean phase direction and magnitude.

c. Rayleigh Z scores of spike-phases for all task-responsive pyramidal cells phase-locked to the beta rhythm locally and cross-regionally on correct versus incorrect trials. (signed-rank tests, CA1 cells phase locked to CA1 beta: n = 28 cells, p = 0.03*; PFC-PFC: n = 8 cells, p = 0.008**, CA1-PFC: n = 18 cells, p = 0.40; PFC-CA1: n = 12 cells, p = 0.20).

d. As in (c), but for spike-phases for all pyramidal cells phase-locked to local RR. (signed-rank tests, CA1-CA1: n = 103 cells, p = 0.04*; PFC-PFC: n = 21 cells, p = 0.24; CA1-PFC: n = 85 cells, p = 0.27; PFC-CA1: n = 49 cells, p = 0.30).

e. Percentage of cells in CA1 and PFC that were phase locked to either beta or RR (z-tests for proportions; CA1: n = 37 cells phase-locked to beta, n = 112 cell phase-locked to RR, z = -9.8, p = 3.2e-20; PFC: n = 17 cells phase-locked to beta, n = 60 cells phase-locked to RR, z = -5.5, p = 1.8e-8).

f. Percentage of cells that are choice-selective (solid bars), phase-locked to the beta rhythm (outlined bars), and both choice-selective and phase-locked (striped bars). Grey bars indicate chance level of cells being both choice-selective and phase-locked, error bars indicate the range of cell percentages that fall within the 95% bounds of the chance binomial distribution. (binomial test, CA1: p = 0.08; PFC: p = 0.16).

g. Polar histogram of preferred beta phases for all task-responsive CA1 interneurons phase-locked to the local CA1 beta rhythm (top, n = 44 cells, z = 8.0, p = 2.9e-4***) and CA1 interneurons phase-locked to the PFC beta rhythm (bottom, n = 25 cells, z = 22.5, p = 1.8e-11***) Arrows indicate mean phase direction and magnitude.

h. Rayleigh Z scores of spike-phases for all task-responsive CA1 interneurons phase-locked locally and cross-regionally to the beta rhythm on correct versus incorrect trials. (signed-rank tests, CA1-CA1: n = 44 cells, p = 8.2e-9***; CA1-PFC: n = 25 cells, p = 1.2e-5***).

i. As in (f), but for interneurons. (binomial test; CA1: p = 0.11; PFC: p = 0.20)

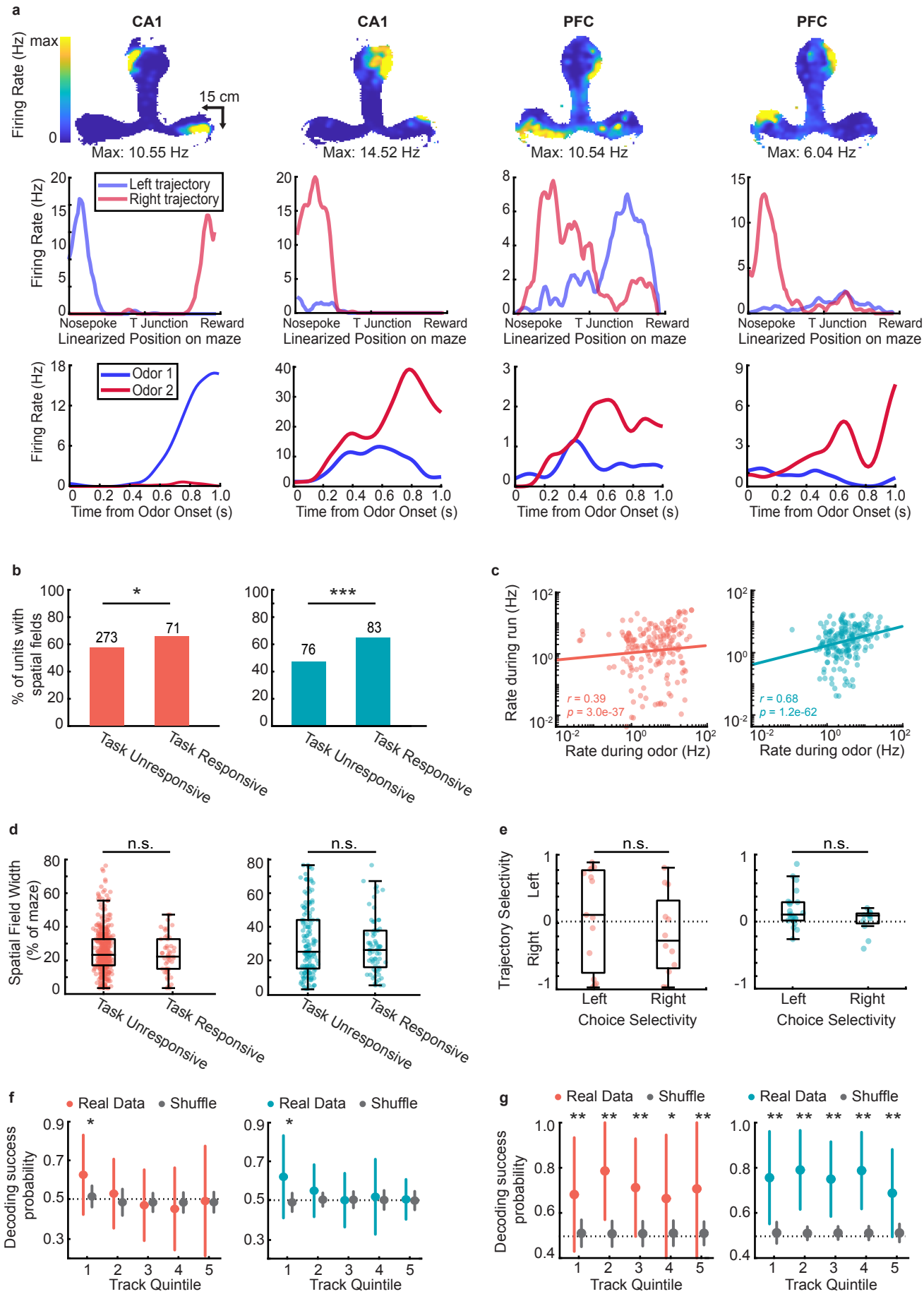
a
CA1
CA1
PFC
PFC
Firing Rate (Hz)
max
0
15 cm
Max: 10.55 Hz
Max: 14.52 Hz
Max: 10.54 Hz
Max: 6.04 Hz
Left trajectory
Right trajectory
Nosepoke
T Junction
Reward
Linearized Position on maze
Odor 1
Odor 2
Time from Odor Onset (s)
b
% of units with spatial fields
273
71
76
83
Task Unresponsive
Task Responsive
c
Rate during run (Hz)
Rate during odor (Hz)
r = 0.39
p = 3.0e-37
r = 0.68
p = 1.2e-62
d
Spatial Field Width (% of maze)
n.s.
e
Trajectory Selectivity
Left
Right
Choice Selectivity
f
Real Data
Shuffle
Decoding success probability
Track Quintile
g

Figure 6: Representations of choice and space are maintained independently during delay period

a. Example choice-selective units (CA1, first two columns, PFC, last two columns) with spatial fields on the track. Top row: Heat map illustrating spatial fields during run bouts. Middle row: Linearized spatial tuning curves for outbound left and right run trajectories. Bottom row: PSTHs showing odor responses during decision-making period (Odor selectivity indices, left to right: 0.92, -0.43, -0.40, -0.57).
b. Spatial field prevalence in task-unresponsive and task-responsive cells in CA1 (left) and PFC (right). CA1: 273/477 (57%) of task-unresponsive cells, and 71/108 (66%) of task-responsive cells had spatial fields (binomial test: p = 0.03*); PFC: 76/160 (48%) of task-unresponsive cells, and 83/128 (66%) of task-responsive cells had spatial fields (binomial test: p = 2.7e-5***).

c. Correlation between firing rates during run and firing rates during odor sampling period for all putative pyramidal cells in CA1 (left) and PFC (right). (CA1: n = 585 cells, r = 0.39, p = 3.0e-37; PFC: n = 288 cells, r = 0.68, p = 1.2e-62).
d. Spatial field width for odor unresponsive and odor responsive units in CA1 (left) and PFC (right). If a unit had a spatial field on both outbound trajectories, each field was counted separately. (Rank-sum tests; CA1: n = 452 fields, p = 0.15; PFC: n = 207 fields, p = 0.92).
e. Trajectory selectivity scores of choice-selective units according to preferred choice (Rank sum tests, CA1: p = 0.26; PFC: p = 0.20).
f. Decoding of choice identity by naïve Bayesian classifier according to CA1 (left) and PFC (right) task-responsive ensemble activity at five equally sized spatial quintiles along the full run trajectory of the maze. 1 spatial quintile = 24.6 cm (123 cm / 5). Colored error bars indicate real data mean ± s.d. whereas grey error bars indicate shuffled data mean ± s.d.

Stars indicate quintiles where the fraction of correctly decoded trials was significantly higher than the fraction from the shuffled data (rank-sum tests, * = $p < 0.05$).

g. As in (f), but decoding of choice identity according to CA1 (left) and PFC (right) spatially-modulated ensemble activity at each spatial quintile. (rank-sum tests, * = $p < 0.05$, ** = $p < 0.01$).